ELSEVIER

Modeling dynamic plasticity and spall fracture in high density polycrystalline alloys

J.D. Clayton *

Impact Physics Branch, US Army Research Laboratory, AMSRD-ARL-WM-TD, Aberdeen Proving Ground, MD 21005-5069, United States

Abstract

The dynamic thermomechanical response of a tungsten heavy alloy is investigated via modeling and numerical simulation. The material of study consists of relatively stiff pure tungsten grains embedded within a more ductile matrix alloy comprised of tungsten, nickel, and iron. Constitutive models implemented for each phase account for finite deformation, heat conduction, plastic anisotropy, strain-rate dependence of flow stress, thermal softening, and thermoelastic coupling. The potentially nonlinear volumetric response in tungsten at large pressures is addressed by a pressure-dependent effective bulk modulus. Our framework also provides a quantitative prediction of the total dislocation density, associated with cumulative strain hardening in each phase, and enables calculation of the fraction of plastic dissipation converted into heat energy. Cohesive failure models are employed to represent intergranular fracture at grain and phase boundaries. Dynamic finite element simulations illustrate the response of realistic volume elements of the polycrystalline microstructure subjected to compressive impact loadings, ultimately resulting in spallation of the material. The relative effects of mixed-mode interfacial failure criteria, thermally-dependent fracture strengths, and grain shapes and orientations upon spall behavior are weighed, with interfacial properties exerting a somewhat larger influence on the average pressure supported by the volume element than grain shapes and initial lattice orientations within the bulk material. Spatially resolved profiles of particle velocities at the free surfaces of the volume elements indicate the degree to which the incident and reflected stress waves are altered by the heterogeneous microstructure.
Published by Elsevier Ltd.

Keywords: Plasticity; Alloys; Thermomechanical; Dynamic; Microstructure

---

* Tel.: +1 410 306 0975; fax: +1 410 306 0783.
 E-mail address: jclayton@arl.army.mil

1. Introduction

Because tungsten heavy alloys (WHAs) typically exhibit a relatively large mass density, high melting point, and high failure strength at elevated rates of loading, these materials are appealing for implementation in long-rod kinetic energy penetration applications (Magness, 1994; Cai et al., 1995). The particular material investigated here consists of pure tungsten grains (BCC) embedded in a polycrystalline matrix phase (FCC) comprised of nickel (50 wt.%), iron (25 wt.%), and tungsten (25 wt.%). Fabrication of the composite material is conducted by isostatic pressing and sintering of a mixture of W, Ni, and Fe powders, followed by an annealing step to remove absorbed hydrogen and then possible quenching, swaging, and/or pre-twisting to alter the dynamic mechanical properties prior to deformation testing at high strain rates (Weerasooriya, 1998; Wei et al., 2000). Typical grain sizes are 10–30 μm for the W crystals and 200–500 μm for the matrix phase (Zhou, 1993), meaning that multiple W crystals are often embedded within each single ''grain'' of the matrix phase.

Macroscopic constitutive models (cf. Stevens and Batra, 1998; Wei et al., 2001) previously used to represent the two-phase system in numerical simulations lack a rigorous description of the kinematics of anisotropic plasticity (e.g. plastic spin), the role of lattice orientations of constituent grains, and the effects of crystal morphology on failure processes. Microstructural characteristics such as grain shape, spatial arrangement of grains, and local crystallographic orientation are known to influence the material's thermomechanical response. Furthermore, experimental (Bruchey et al., 1991, 1992) and numerical (Schoenfeld and Benson, 1997) studies have suggested a possible correlation between the lattice orientation of W single crystals and the performance of such crystals as kinetic energy penetrators. Previous computational work by Zhou and co-workers (Zhou et al., 1994; Zhou, 1998) explained the influences of grain morphology, heat conduction, strain- and strain-rate hardening, and thermal softening on the elastoplastic deformation and shear localization of tungsten alloys at high rates of shear and combined pressure-shear loading. While grain and matrix phases were resolved discretely in these calculations, each constituent was treated as an isotropically-hardening, hypothermoelastic–viscoplastic material, thus neglecting possibly significant effects of lattice rotation and anisotropic strain hardening associated with the evolution of crystallographic texture. In contrast, in the present investigation we employ a crystal plasticity framework (cf. Asaro, 1983) to examine the effects of crystallographic orientation and plastic anisotropy.

When subjected to tensile states of stress, tungsten alloys are known to fracture readily along grain and phase boundaries (Zamora et al., 1992; Woodward and O'Donnell, 2000; Weerasooriya, 2003). Weerasooriya (2003) deduced that failure of WHA specimens subjected to high rates of tensile deformation often initiates via fracture at W–W interfaces, and less often at interfaces between W grains and the matrix phase. The former interfaces are often thought to be weaker than the latter, based upon visual examination of recovered specimens that demonstrate how fracture surfaces are prone to initiate at W–W boundaries and then either propagate along W–matrix interfaces, or less frequently, along cleavage planes within grains of either phase (Zamora et al., 1992; Weerasooriya et al., 1994; O'Donnell and Woodward, 2000; Woodward and O'Donnell, 2000; Weerasooriya, 2003). O'Donnell and Woodward (2000) noted that at higher ambient temperatures (>373 K), the tendency for cleavage fracture within grains tends to increase at the expense of interfacial fracture. Zamora et al. (1992) observed that microscopic fracture mechanisms and macroscopic fracture toughness measurements in such alloys vary widely with chemical composition, grain size, and grain continuity. In our constitutive framework and associated numerical scheme, we address interfacial fracture through cohesive zone models (Barenblatt, 1959; Camacho and Ortiz, 1996). Thus we are able to capture a failure mode that may dominate the response of the WHA system under tensile stress states, in contrast to prior computational studies reported in the literature that did not treat fracture explicitly.

In the present work we investigate tensile fractures emerging in the setting of a numerical wave propagation simulation (cf. Espinosa and Zavattieri, 2003a,b). A finite sample of the material is subjected to a

compressive pressure pulse which subsequently traverses the sample and then reflects off of its free surface as a tensile wave, leading to spall failure within the sample. Dandekar (1976) and Asay et al. (1980) studied the shock behavior of pure polycrystalline tungsten. The high pressure responses, including spallation, of various W alloys were probed experimentally via plate impact testing by Dandekar and Weisgerber (1999) and through explosive loading by Baoping et al. (1994). The former researchers (Dandekar and Weisgerber, 1999) found the spall stress of WHAs to be nearly independent of impact stress over a range of 5.9–24 GPa, attaining values of 1.9 ± 0.4 GPa, whereas the latter (Baoping et al., 1994) reported an increase in spall strength of WHAs from 0.54 GPa to 3 GPa when shocked to applied stress levels between 21 and 30 GPa, followed by a decrease in strength to 1.56 GPa at an applied pressure of 32 GPa. Baoping et al. (1994) noted that atomic diffusion or phase changes may affect the response of the material at extremely high pressures, as may a transition in dominant failure mechanism from intragranular to intergranular fractures, or vice-versa.

The present study employs single crystalline plasticity models for the bulk response of each phase, as detailed in Section 2. Constitutive models for both materials are embedded within a general thermodynamic framework applicable for describing any thermoelastic–viscoplastically-deforming metallic crystal. The description accounts for finite deformation and volume change, strain-rate dependence, heat conduction, thermal expansion, thermal softening, and thermoelastic coupling. Furthermore, our framework enables calculation of the percentage of plastic work stored in the material as residual elastic energy associated with lattice defects (i.e., dislocations). As discussed in Section 3, cohesive zone models accounting for failure strengths depending upon mode mixity and temperature represent the constitutive behavior in damaged regions at intergranular interfaces. Finite element meshes of equiaxed grains and elongated grains are constructed, corresponding to transverse and longitudinal sections, respectively, of samples of WHA material cut from an actual kinetic energy penetrator. Experimentally-measured crystallographic textures and randomly-generated textures are also varied as initial conditions in the simulations. Polycrystals are subjected to high-rate uniaxial compression leading to spall fracture, with results of these simulations described in Section 4.

2. Crystal plasticity formulation

2.1. Kinematics

Let $\mathbf{x} = \mathbf{x}(\mathbf{X}, t)$ represent a smooth time-dependent motion, with $\mathbf{x}$ and $\mathbf{X}$ spatial and reference coordinates, respectively. The local deformation gradient $\mathbf{f}$ is decomposed as

$$\mathbf{f} \equiv \frac{\partial \mathbf{x}}{\partial \mathbf{X}} = \mathbf{f}^e \mathbf{f}^\theta \mathbf{f}^p, \tag{1}$$

where $\mathbf{f}^e$, $\mathbf{f}^\theta$, and $\mathbf{f}^p$ represent, respectively, the kinematics of elasticity and rigid-body rotation, stress-free thermal expansion or contraction, and the cumulative contribution of moving crystal defects. In Eq. (1) and henceforward, juxtaposition implies summation over one set of adjacent indices, i.e., $(\mathbf{AB})^i_{.k} = A^i_{.j} B^j_{.k}$ for any second-rank tensors $\mathbf{A}$ and $\mathbf{B}$. During arbitrarily heterogeneous plastic flow, none of $\mathbf{f}^e$, $\mathbf{f}^\theta$, and $\mathbf{f}^p$ is a compatible (i.e., integrable) deformation gradient. As shown in Fig. 1, the elastic and thermal terms dictate the deformation of the slip direction contravariant vectors $\mathbf{s}^{(\alpha)}$ and slip plane normal covariant vectors $\mathbf{m}^{(\alpha)}$:

$$\mathbf{s}^{(\alpha)} = \mathbf{f}^e \mathbf{f}^\theta \mathbf{s}_0^{(\alpha)}, \quad \mathbf{m}^{(\alpha)} = \mathbf{m}_0^{(\alpha)} \mathbf{f}^{\theta-1} \mathbf{f}^{e-1}, \tag{2}$$

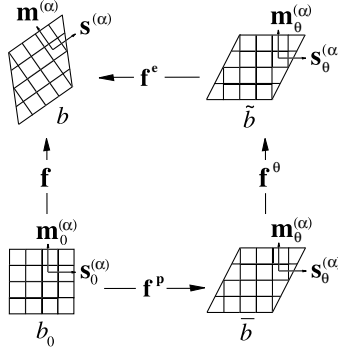with the superposed "−1" denoting matrix inversion. The spatial velocity gradient $\mathbf{l}$ is written as

Fig. 1. Deformations, configurations, and slip vectors.

$$\mathbf{l} \equiv \frac{\partial \dot{\mathbf{x}}}{\partial \mathbf{x}} = \dot{\mathbf{f}}\mathbf{f}^{-1} = \underbrace{\dot{\mathbf{f}}^e \mathbf{f}^{e-1}}_{\equiv \mathbf{l}^e} + \underbrace{\mathbf{f}^e \dot{\mathbf{f}}^\theta \mathbf{f}^{\theta-1} \mathbf{f}^{e-1}}_{\equiv \mathbf{l}^\theta} + \underbrace{\mathbf{f}^e \mathbf{f}^\theta \dot{\mathbf{f}}^p \mathbf{f}^{p-1} \mathbf{f}^{\theta-1} \mathbf{f}^{e-1}}_{\equiv \mathbf{l}^p}, \tag{3}$$

where the superposed dot implies a material time derivative. As we are concerned here with cubic lattices, thermal deformation is assumed isotropic (Lee et al., 1997)

$$\mathbf{l}^\theta = \dot{\mathbf{f}}^\theta \mathbf{f}^{\theta-1} = \alpha_\mathrm{T} \dot\theta \mathbf{1}, \tag{4}$$

where θ is the temperature change measured from the reference state and $\alpha_\mathrm{T}(\theta)$ is the temperature-dependent thermal expansion coefficient giving the change in length per unit current length per unit increment in θ. The unit tensor is denoted by $\mathbf{1}$. The plastic velocity gradient in the intermediate configuration $\bar{b}$ of Fig. 1 is defined as in classical crystal plasticity theory (Asaro, 1983):

$$\bar{\mathbf{l}}^p \equiv \dot{\mathbf{f}}^p \mathbf{f}^{p-1} = \sum_{\alpha=1}^n \dot\gamma^{(\alpha)} \mathbf{s}_0^{(\alpha)} \otimes \mathbf{m}_0^{(\alpha)}, \tag{5}$$

with $\dot\gamma^{(\alpha)}$ the plastic shearing rate on slip system α, n the number of potentially active slip systems, and $\otimes$ the tensor product. As a result of the orthogonality of $\mathbf{s}_0^{(\alpha)}$ and $\mathbf{m}_0^{(\alpha)}$, the plastic deformation is volume-preserving, i.e. $\mathrm{tr}\bar{\mathbf{l}}^p = 0$, where the trace operation for a second rank tensor $\mathbf{A}$ is denoted by $\mathrm{tr}(\mathbf{A}) = A^k_{.k}$.

2.2. Balance laws

Localized balance laws are specified in the current configuration as follows:

$$\dot\rho + \rho\,\mathrm{tr}(\mathbf{l}) = 0, \quad \mathrm{div}\,\boldsymbol\sigma + \rho\mathbf{b} = \rho\ddot{\mathbf{x}}, \quad \boldsymbol\sigma = \boldsymbol\sigma^\mathrm{T}, \quad \rho\dot{e} + \mathrm{div}\,\mathbf{q} - \mathrm{tr}(\boldsymbol\sigma\mathbf{g}\mathbf{l}) = \rho r, \tag{6}$$

with ρ, $\boldsymbol\sigma$, $\mathbf{b}$, e, $\mathbf{q}$, and r denoting the current mass density, contravariant Cauchy stress tensor, body force vector per unit mass, internal energy per unit mass, heat flux vector per unit current area, and energy source per unit mass, respectively. We use 'div' to represent divergence with respect to spatial coordinates, for example $\mathrm{div}\,\mathbf{q} = q^a_{|a} = \partial_a q^a + \gamma^a_{ab} q^b$ with the usual Christoffel symbols in the spatial coordinate system satisfying $2g_{ad}\gamma^d_{bc} = \partial_c g_{ba} + \partial_b g_{ca} - \partial_a g_{cb}$, where the compact notation $\partial_a = \partial/\partial x^a$ and the spatial metric satisfies $g_{ab} = \partial_a \mathbf{x} \cdot \partial_b \mathbf{x}$. The local entropy inequality is written as follows, with $\dot\eta$ the time rate of entropy production per unit mass

$$\rho\dot\eta \geqslant -\mathrm{div}\left(\frac{\mathbf{q}}{\theta}\right) + \frac{\rho r}{\theta}. \tag{7}$$

Next introduced is the Helmholtz free energy per unit mass, ψ:

$$\psi \equiv e - \theta\eta. \tag{8}$$

Subsequently, upon substitution of (6) and (8) into (7), the entropy inequality becomes

$$\mathrm{tr}(\boldsymbol{\sigma}\mathbf{gl}) - \frac{\mathbf{q} \cdot \nabla_x\theta}{\theta} \geqslant \rho(\dot{\psi} + \dot{\theta}\eta), \tag{9}$$

with $\nabla_{\mathbf{x}}\theta$ the contravariant temperature gradient in the spatial frame and $\cdot$ a scalar product operation for vectors, e.g., $\mathbf{a}\cdot\mathbf{b} = a^i g_{ij} b^j$.

2.3. Thermodynamic framework

We assume a Helmholtz free energy potential of the form

$$\psi = \psi(\mathbf{e}^e, \theta, \xi), \tag{10}$$

where the intermediate configuration elastic strain $2(e^e)_{\alpha\beta} = f^{ea}_{.\alpha} g_{ab} f^{eb}_{.\beta} - \tilde{g}_{\alpha\beta}$, with $\tilde{g}_{\alpha\beta}$ a metric tensor on $\tilde{b}$, which in practice is chosen as Kronecker's delta $\delta_{\alpha\beta}$ for simplicity (Simo and Ortiz, 1985), a typical assumption in finite elastoplasticity theory (Clayton et al., 2004). The symbol ξ denotes a dimensionless scalar internal variable representing stored micro-elastic energy associated with crystal defects that may impede shearing on each slip system. Expanding the time rate of ψ and inserting the result into inequality (9) yields

$$\mathrm{tr}(\boldsymbol{\sigma}\mathbf{g}(\mathbf{l}^e + \mathbf{l}^\theta + \mathbf{l}^p)) - \frac{\mathbf{q} \cdot \nabla_x\theta}{\theta} \geqslant \rho(\partial_{\mathbf{e}^e}\psi\dot{\mathbf{e}}^e + (\partial_\theta\psi)\dot{\theta} + (\partial_\xi\psi)\dot{\xi} + \dot{\theta}\eta), \tag{11}$$

where the scalar product of two second rank objects is defined by $\mathbf{A}:\mathbf{B} = A^{ij}B_{ij}$, and where the subscript following the ∂-operator denotes partial differentiation with respect to the subscripted variable. Additional algebraic manipulations give

$$\frac{\rho}{\tilde{\rho}}(\mathbf{s}^e - \tilde{\rho}\partial_{\mathbf{e}^e}\psi) : \dot{\mathbf{e}}^e + (\mathrm{tr}(\boldsymbol{\sigma}\mathbf{g})\alpha_{\mathrm{T}} - \rho(\partial_\theta\psi) - \rho\eta)\dot{\theta} - \rho(\partial_\xi\psi)\dot{\xi} + \sum_{\alpha=1}^{n}\tau^{(\alpha)}\dot{\gamma}^{(\alpha)} \geqslant \frac{\mathbf{q} \cdot \nabla_x\theta}{\theta}, \tag{12}$$

where $\tilde{\rho}$ is the mass density in configuration $\tilde{b}$ and the elastic second Piola–Kirchhoff stress $(s^e)^{\alpha\beta} \equiv j^e f^{e-1\alpha}_{.a}\sigma^{ab} f^{e-1\beta}_{.b}$ with $j^e \equiv \tilde{\rho}/\rho = \det\mathbf{f}^e$. The resolved Cauchy stress on slip system α is found by $\tau^{(\alpha)} \equiv \boldsymbol{\sigma}:(\mathbf{gs}^{(\alpha)}\otimes\mathbf{m}^{(\alpha)})$. Assuming that the elastic strain $\mathbf{e}^e$ and temperature θ can be varied apart from the inelastic rates $\dot{\gamma}^{(\alpha)}$ and $\dot{\xi}$ (cf. Coleman and Noll, 1963), (12) is satisfied when

$$\mathbf{s}^e = \tilde{\rho}\partial_{\mathbf{e}^e}\psi, \tag{13}$$

$$\eta = \underbrace{\frac{\alpha_{\mathrm{T}}}{\rho}\mathrm{tr}(\boldsymbol{\sigma}\mathbf{g})}_{\equiv\chi} - \partial_\theta\psi, \tag{14}$$

$$\sum_{\alpha=1}^{n}\tau^{(\alpha)}\dot{\gamma}^{(\alpha)} - \rho(\partial_\xi\psi)\dot{\xi} \geqslant \frac{\mathbf{q} \cdot \nabla_x\theta}{\theta}. \tag{15}$$

Notice that the first term on the right of (14), denoted by χ, arises as a consequence of the explicit inclusion of thermal deformation in the kinematic description (1). Rearranging the energy balance in (6) by appealing to (13) and (14) gives

$$\rho\theta\dot{\chi} - \rho\theta\partial_\theta\dot{\psi} = \rho r - \mathrm{div}\mathbf{q} + \sum_{\alpha=1}^{n}\tau^{(\alpha)}\dot{\gamma}^{(\alpha)} - \rho(\partial_\xi\psi)\dot{\xi}. \tag{16}$$

The specific heat capacity $\hat{c}$ is defined as

$$\hat{c} \equiv \partial_\theta e = \partial_\eta e(\partial_\theta \eta) = -\theta, (\partial_{\theta\theta}\psi) + \partial_\eta e \partial_\theta \chi \tag{17}$$

where we have invoked the differential of relation (8). Assuming isotropic heat conduction in the spatial frame dictated by Fourier's law (Zhou et al., 1994)

$$\mathbf{q} = -k\nabla_x\theta \tag{18}$$

with $k(\mathbf{x}, \theta)$ the spatial thermal conductivity, we can rewrite the localized energy balance (16) as

$$\underbrace{\rho\hat{c}\dot{\theta}}_{\text{temperature change}} = \underbrace{\sum_{\alpha=1}^n \tau^{(\alpha)}\dot{\gamma}^{(\alpha)}}_{\text{plastic dissipation}} - \underbrace{\rho((\partial_\xi\psi) - \theta(\partial_{\theta\xi}\psi))\dot{\xi}}_{\text{energy of lattice defects}} + \underbrace{\rho\theta\partial_{\theta e^e}\psi : \dot{\mathbf{e}}^e}_{\text{thermoelastic coupling}} + \underbrace{\text{div}(k\nabla_x\theta)}_{\text{heat conduction}} + \underbrace{\rho r}_{\text{heat supply}}. \tag{19}$$

2.4. Constitutive theory

A free energy potential per unit intermediate configuration volume is specified as

$$\tilde{\rho}\psi = \frac{1}{2}K_0(\theta)\vartheta^2 - \frac{1}{3}K_1\vartheta^3 + \mu(\theta)\mathbf{e}^{e'} : \mathbf{e}^{e'} + \frac{1}{2}\kappa\mu(\theta)\xi^2 + y(\theta), \tag{20}$$

where $\vartheta \equiv \text{tr}(\mathbf{e}^e)$ measures the elastic volume change, K_0, K_1, and μ are elastic stiffness constants and κ is a dimensionless, material-dependent scalar parameter that we assume is independent of strain rate and temperature. We shall later demonstrate the explicit relationship between κ and the fraction of plastic dissipation converted to heat energy (Eq. (37)). The covariant deviatoric elastic strain tensor in the intermediate frame is defined by $\mathbf{e}^{e'} \equiv \mathbf{e}^e - (1/3)\vartheta\tilde{\mathbf{g}}$. The function $y(\theta) = -\hat{c}\theta\ln(\theta/\theta_0)$ accounts for the purely thermal energy (Rosakis et al., 2000), with θ_0 a reference temperature at which $y = 0$. From Eq. (13) and partial differentiation of (20), we see that the stress tensor satisfies

$$\mathbf{s}^e = \tilde{\rho}\partial_{\mathbf{e}^e}\psi = \underbrace{(K_0 - K_1\vartheta)}_{\equiv \tilde{K}}\vartheta\tilde{\mathbf{g}}^{-1} + 2\mu\tilde{\mathbf{g}}^{-1}\mathbf{e}^{e'}\tilde{\mathbf{g}}^{-1}, \tag{21}$$

where $\tilde{K}$ is the temperature- and volume-dependent (i.e., pressure-dependent) effective bulk modulus. The hydrostatic pressure $\tilde{p}$ and deviatoric stress $\mathbf{s}^{e'}$ in the intermediate frame become, from (21),

$$\tilde{p} \equiv -\frac{1}{3}\text{tr}(\mathbf{s}^e) = -\tilde{K}\vartheta, \quad \mathbf{s}^{e'} \equiv \mathbf{s}^e + \tilde{p}\tilde{\mathbf{g}}^{-1} = 2\mu\tilde{\mathbf{g}}^{-1}\mathbf{e}^{e'}\tilde{\mathbf{g}}^{-1}. \tag{22}$$

Thermoelastic properties for W and binder phases are listed in Table 1, where the temperature change is defined by $\Delta\theta \equiv \theta - 273$ K. The dependencies of the elastic moduli, conductivity, specific heat, and coeffi-

Table 1
Thermoelastic properties

Property	Value (W)	Value (matrix)
μ	$160.3 - 0.0146(\Delta\theta) - 0.0000033(\Delta\theta)^2$ GPa	99.0 GPa
K_0	$310.8 - 0.01759(\Delta\theta) - 0.0000003(\Delta\theta)^2$ GPa	190.3 GPa
K_1	1450 GPa	–
α_T	$5.3(10)^{-6} + 1.584(10)^{-9}\ (\Delta\theta)$/K	$1.5(10)^{-5}$/K
$\hat{c}$	$135.8(1 - 4805/\theta^2) + 0.00912\theta + 0.00231(10)^{-6}\theta^3$ J/(kg K)	382 J/(kg K)
k	$160 - 0.05(\Delta\theta)$ W/(m K)	100 W/(m K)
ρ_0	19350 kg/m^3	9200 kg/m^3

cient of thermal expansion of the pure W phase on temperature were obtained from Yih and Wang (1979), most valid for $\theta \leqslant 1500$ K. Temperature and pressure dependencies of thermoelastic properties of the matrix phase are unknown and were neglected in the computations. The value of the bulk modulus term K_1 was obtained from a linear fit to the data of Ruoff et al. (1998), most valid for applied pressures less than 35 GPa. In the final row of Table 1, the mass density in the reference configuration is written as ρ_0, with the listed value corresponding to a reference temperature of $\theta = 300$ K.

Note that single crystalline W is unusual in the sense that it is elastically isotropic at the reference temperature and low pressures. Presumably, single crystals of the FCC binder phase are not elastically isotropic; however, we resort here to isotropic stiffness constants obtained from elastic wave speed measurements on polycrystalline sample (Zhou, 1993), as anisotropic stiffness constants are presently unavailable for single crystals of the binder phase. Note also that pressure dependency of the shear moduli is neglected here, as this effect is relatively unimportant in the present context where plasticity dominates the deviatoric stress–strain response. On the other hand, a volume-dependent bulk modulus is necessary in order to numerically capture the sharpening of elastic stress waves into a shock discontinuity commensurate with the increase in wave speed occurring in highly compressed material behind a pressure front (Becker, 2004). Our implementation is relatively simple, involving only a linear dependence of bulk modulus on elastic volume change and a quadratic dependency of stiffness upon temperature. This approach is deemed sufficient over the present range of simulation conditions ($\tilde{p} < 0.1\,K_0$). More robust formulations involving equations-of-state (cf. Grüneisen, 1926) and pressure derivatives of shear moduli may be necessary for modeling elastically anisotropic crystals deformed at pressures on the order of the reference bulk modulus—see for example simulations of polycrystalline tantalum by Becker (2004). Note also that the stiffness constants and elastic volume change ϑ are defined with respect to the *intermediate* configuration, a conventional practice in finite crystal plasticity theory (Asaro, 1983). This poses no conceptual difficulties and is rigorous if the material parameters are determined in a manner consistent with their definitions. However, in experiments the constants are often determined by perturbing the material from its equilibrium state in the *current* configuration. Specifically, data used to determine the volume-dependent parameter K_1 (Ruoff et al., 1998) were given in terms of Cauchy pressure $p \equiv -(1/3)\,\mathrm{tr}\,\boldsymbol{\sigma}$ and elastic volume change per unit reference volume in the absence of plasticity or thermal expansion, $j^e - 1$. The final value of K_1 appearing in Table 1 was found from a conversion using the relations $\vartheta = 1.017(j^e - 1)$ and $p = 1.036\tilde{p}$ when $j^e = 0.9$, corresponding to a 10% volumetric reduction at an applied Cauchy pressure of 36.6 GPa. The linear elasticity constants (K_0 and μ) of Table 1 correspond to those measured at small elastic strains, i.e. when $j^e \approx 1$.

Our decomposition of the deformation gradient into distinct elastic and thermal terms differs somewhat from usual finite thermoelasticity (cf. Marsden and Hughes, 1983). Consider a purely thermoelastic process at a material point where the total deformation is prohibited, such that $\mathbf{f} = \mathbf{f}^e \mathbf{f}^\theta = \mathbf{1}$, and the temperature is increased above its reference value. Then due to thermal expansion, $\det \mathbf{f}^\theta > 1$, and in order to compensate and maintain null total strain, $\det \mathbf{f}^e < 1$ and hence $\vartheta < 0$, resulting in a positive pressure $\tilde{p} > 0$ from (22).

Plasticity models are discussed next. A power-law viscoplastic flow rule (Hutchinson, 1976) is chosen to model the time rate of plastic deformation within each phase of the bulk material:

$$\dot{\gamma}^{(\alpha)} = \dot{\gamma}_0 \left(\frac{\tilde{\tau}^{(\alpha)}}{g^{(\alpha)}} \right)^m \mathrm{sgn}(\tilde{\tau}^{(\alpha)}). \tag{23}$$

Here $\dot{\gamma}_0$ and m are material parameters, $g^{(\alpha)}$ is the slip resistance due to dislocation barriers, $\tilde{\tau}^{(\alpha)} \equiv j^e \tau^{(\alpha)}$ is the projected shear stress pulled back to the intermediate configuration $\tilde{b}$ of Fig. 1, and $\mathrm{sgn}(x) = x/|x|$, with $\mathrm{sgn}(0) = 1$. Thermal softening attributed to increased dislocation mobility at high temperatures is incorporated via the power-law form (Klopp et al., 1985)

$$g^{(\alpha)} = g_0^{(\alpha)} (\theta/\theta_0)^p, \tag{24}$$

with $g_0^{(\alpha)}$ the flow resistance at reference temperature θ_0 (a material parameter) and p a dimensionless constant for each material. We postulate the following relationship between the "average" hardening over all systems at fixed reference temperature and the internal variable ξ:

$$\frac{1}{n} \sum_{\alpha=1}^{n} (g_0^{(\alpha)} - g_y^{(\alpha)}) = \hat{\alpha} \mu(\theta_0) \underbrace{b \sqrt{\rho_{\mathrm{T}}}}_{\equiv \xi}, \tag{25}$$

with $g_y^{(\alpha)}$ an initial yield stress, b the magnitude of the Burgers vector in the reference lattice, and ρ_{T} the total dislocation line length per unit intermediate configuration volume associated with shearing impedance. The square-root dependence of flow stress on dislocation density is a typical assumption in the plasticity and materials science literature (Taylor, 1934; Kuhlmann-Wilsdorf, 1985; Zikry and Kao, 1996), as is the assertion of linear dependence of stored lattice energy on dislocation density (Bammann, 2001; Svendsen, 2002) implied jointly by Eqs. (20) and (25). The scalar proportionality factor $\hat{\alpha}$ accounts for dislocation interactions (Kobytev et al., 1984; Ashmawi and Zikry, 2003). Both lattice friction stress (Qiu et al., 2001) and effects of initial dislocation density are incorporated in the initial yield stress $g_y^{(\alpha)}$.

Specifically for pure W crystals, we allow slip in the $\langle 111 \rangle$ close-packed directions on any of the $\{110\}$ and $\{112\}$ families of planes, meaning the number of potentially active slip systems is $n = 24$ (Subhash et al., 1994). Possible slip on $\{123\}$ families of planes, thought to be inactive at room temperature (Argon and Maloof, 1966; Subhash et al., 1994), is not represented in our model. Evolution of slip resistance at reference temperature θ_0 is dictated by a hardening-minus-dynamic-recovery relation reminiscent of a form introduced in a macroscopic plasticity setting by Armstrong and Frederick (1966) and more recently used in a crystal plasticity framework by Horstemeyer et al. (1999):

$$\dot{g}_0^{(\alpha)} = A \sum_{\beta=1}^{n} q_\beta^\alpha \mid \dot{\gamma}^{(\beta)} \mid - B g_0^{(\alpha)} \sum_{\beta=1}^{n} \mid \dot{\gamma}^{(\beta)} \mid, \tag{26}$$

with the interaction matrix satisfying

$$q_\beta^\alpha = \delta_\beta^\alpha + q(1 - \delta_\beta^\alpha), \tag{27}$$

where q is the latent hardening ratio. Material parameters for the plasticity models are compiled in Table 2. As calibrations to experimental data used to obtain these parameters are discussed in detail in a previous publication by the author (Clayton, 2005), only a brief overview is given here. Values of $g_y^{(\alpha)} = g_0^{(\alpha)}|_{t=0}$, A, and B in Eq. (26) were chosen to fit the quasi-static compression data for polycrystalline W of Dümmer et al. (1998), and a relatively large value of $q = 1.4$ was selected for implementation in Eq. (27) following the discussion on strong latent hardening in W single crystals by Horwath (1994). Strain rate and thermal

Table 2
Properties for inelastic material response

Parameter	Value (W)	Value (matrix)
$\dot{\gamma}_0$	0.001	0.001
m	20	20
q	1.4	1.0
A	630 MPa	200 MPa
B	1.5	0.4
$g_y^{(\alpha)}$	500 MPa	150 MPa
p	−1.5	−1.5
θ_0	300 K	300 K
$\hat{\alpha}$	0.439	1.03
b	0.275 nm	0.257 nm
κ	1333	200

sensitivity parameters, m and p respectively, were obtained from the crystal plasticity model for pure W of Lee et al. (1999). The value of the reference strain rate $\dot{\gamma}_0$, required on dimensional grounds (Hutchinson, 1976), was chosen for convenience during the process of selecting the other parameters. Aggregates of 300 initially randomly-oriented crystals subjected to uniform deformation constraints (Taylor, 1938) in the absence of inertia were used in the calibrations.

In the W–Ni–Fe matrix material, the number of potentially active slip systems was chosen as $n = 12$. We assume that dislocations glide in $\langle 1\,1\,0 \rangle$ close-packed directions on $\{1\,1\,1\}$ planes for this FCC metal. Strain rate- and temperature-dependent slip resistances in crystals comprising the more compliant binder phase evolve via relations (26) and (27), though with different values of A, B, and q than those invoked for the pure W grains. Specifically, constants A and B in (26) and initial conditions $g_y^{(\alpha)} = g_0^{(\alpha)}|_{t=0}$ were chosen to fit the quasi-static ($\dot{\gamma} = 10^{-4}$) torsion data of Zhou (1993), and the strain rate sensitivity exponent was assumed to be the same as that for the pure W grains following the experimental data of Zhou (1993). We also selected $\dot{\gamma}_0$ to match the value for the pure W, and used Taylor's (1934) latent hardening assumption typical for FCC metals, $q = 1.0$. Choices of $\hat{\alpha}$ and κ for each phase are discussed below in Section 2.5.

2.5. Implementation and internal variables

An implicit hyperelastic–viscoplastic algorithm (cf. Cuitiño and Ortiz, 1992) was employed to integrate the elastic–plastic constitutive response. Let subscripts t and $t + \Delta t$ denote consecutive computation times in a nonlinear analysis, i.e., start and end times in a particular iteration cycle. Slip rates for a given increment spanning times t and $t + \Delta t$ are found implicitly from values of the resolved shear stress and hardening variables at the end of the cycle:

$$\dot{\gamma}^{(\alpha)} = \dot{\gamma}_0 \left| \frac{\tilde{\tau}_{t+\Delta t}^{(\alpha)}}{g_{t+\Delta t}^{(\alpha)}} \right|^m \mathrm{sgn}\left(\tilde{\tau}_{t+\Delta t}^{(\alpha)} \right). \tag{28}$$

We use an iterative procedure to solve (28), since $\tilde{\tau}_{t+\Delta t}^{(\alpha)}$ and $g_{t+\Delta t}^{(\alpha)}$ depend upon the solution variables $\dot{\gamma}^{(\alpha)}$. Notice that $\tilde{\tau}_{t+\Delta t}^{(\alpha)}$ and $g_{t+\Delta t}^{(\alpha)}$ depend upon θ, via Eq. (24) and the temperature dependence of elastic moduli. The temperature rate for a given increment spanning t and $t + \Delta t$ is found, from Eq. (19) with $r = 0$, explicitly in terms of quantities at time t:

$$\dot{\theta} = \left(\frac{\beta}{\rho \hat{c}} \sum_{\alpha=1}^{n} \tau^{(\alpha)} \dot{\gamma}^{(\alpha)} + \frac{\theta}{\hat{c}} \partial_\theta (\mathbf{s}^e : \dot{\mathbf{e}}^e) + \frac{1}{\rho \hat{c}} \mathrm{div}(k \nabla_x \theta) \right) \bigg|_t, \tag{29}$$

where

$$\beta \equiv \left(\sum_{\alpha=1}^{n} \tau^{(\alpha)} \dot{\gamma}^{(\alpha)} - \rho((\partial_\xi \psi) - \theta(\partial_{\theta\xi}\psi))\dot{\xi} \right) \left(\sum_{\alpha=1}^{n} \tau^{(\alpha)} \dot{\gamma}^{(\alpha)} \right)^{-1}, \tag{30}$$

meaning that $1 - \beta$ is the ratio of the rate of stored energy of lattice defects to the rate of plastic work (Taylor and Quinney, 1934). In practice, β is often prescribed a fixed magnitude for a particular material regardless of the temperature-deformation history, with $0.8 \leqslant \beta \leqslant 1.0$ typical for engineering metals (Aravas et al., 1990; Zhou et al., 1994). We do not employ this constitutive assumption here. The temperature at time $t + \Delta t$ is updated simply via

$$\theta_{t+\Delta t} = \theta_t + \dot{\theta} \Delta t, \tag{31}$$

and the thermal deformation gradient at the end of the step is found from

$$\mathbf{f}_{t+\Delta t}^{\theta} = \exp(\alpha_{\mathrm{T}} \dot{\theta} \mathbf{1} \Delta t) \mathbf{f}_t^{\theta}, \tag{32}$$

with exp( ) the matrix exponential function and the property α_T in (32) evaluated at $\theta_{t+\Delta t}$. For a given time increment, Eqs. (28) are solved implicitly using values of $\dot{\theta}$, $\theta_{t+\Delta t}$, and $\mathbf{f}_{t+\Delta t}^\theta$ found from (29)–(32). The thermoelastic term in (19), upon assuming $j^\theta \equiv \det \mathbf{f}^\theta \approx 1 + 3\alpha_T(\theta - \theta_0)$ can be rewritten, to first-order, as

$$
\begin{aligned}
\rho\theta\partial_{\theta\mathbf{e}^e}\psi : \dot{\mathbf{e}}^e &= \theta j^{e-1}\partial_\theta(\mathbf{s}^e : \dot{\mathbf{e}}^e) - \rho\theta j^\theta\partial_\theta(j^{\theta-1})(\mathbf{s}^e : \dot{\mathbf{e}}^e) \\
&\approx \theta j^{e-1}\left\{\left[(\partial_\theta\lambda)\tilde{g}^{\alpha\beta}\tilde{g}^{\chi\delta} + (\partial_\theta\mu)(\tilde{g}^{\alpha\chi}\tilde{g}^{\beta\delta} + \tilde{g}^{\alpha\delta}\tilde{g}^{\beta\chi})\right](\dot{e}^e)_{\chi\delta} + 3\alpha_T(j^{\theta-1}s^{e\alpha\beta})\right\}(\dot{e}^e)_{\alpha\beta}.
\end{aligned}
\tag{33}
$$

where for pure W,

$$
\partial_\theta\lambda = -3.4 + 0.0065(\Delta\theta) \text{ MPa/K}, \quad \partial_\theta\mu = -14.6 - 0.0066(\Delta\theta) \text{ MPa/K},
\tag{34}
$$

and where the second of (34) agrees with the form given in Table 1. Temperature dependencies of elastic moduli of the matrix phase are unknown and hence were neglected in the computation of thermoelastic heating effects.

Additional explanation regarding the role of the internal variable state variable ξ, in each phase corresponding to the total dislocation density, is now merited. Manipulating Eq. (25) and then differentiating with respect to time give, respectively,

$$
\xi \equiv b\sqrt{\rho_T} = \frac{\tilde{\rho}\partial_\xi\psi}{\kappa\mu} = \frac{1}{\hat{\alpha}\mu n}\sum_{\alpha=1}^n(g_0^{(\alpha)} - g_y^{(\alpha)}), \quad \dot{\xi} = b\frac{\dot{\rho}_T}{2\sqrt{\rho_T}} = \frac{1}{\hat{\alpha}\mu n}\sum_{\alpha=1}^n\dot{g}_0^{(\alpha)}.
\tag{35}
$$

Additionally,

$$
\tilde{\rho}\theta(\partial_{\theta\xi}\psi) = \theta\partial_\theta(\kappa\mu b\sqrt{\rho_T}) = \kappa\theta(\partial_\theta\mu)(b\sqrt{\rho_T}) = \frac{\kappa\theta(\partial_\theta\mu)}{\hat{\alpha}\mu n}\sum_{\alpha=1}^n\left(g_0^{(\alpha)} - g_y^{(\alpha)}\right).
\tag{36}
$$

Substituting (35) and (36) into (30) then yields

$$
\beta = 1 - \frac{\kappa(\mu + \theta(\partial_\theta\mu))}{(\hat{\alpha}\mu n)^2}\left[\sum_{\alpha=1}^n(g_0^{(\alpha)} - g_y^{(\alpha)})\sum_{\alpha=1}^n\dot{g}_0^{(\alpha)}\right]\left[\sum_{\alpha=1}^n\tilde{\tau}^{(\alpha)}\dot{\gamma}^{(\alpha)}\right]^{-1}.
\tag{37}
$$

The dislocation density variable can be determined from (35) once $\hat{\alpha}$ is known, i.e.,

$$
\rho_T = \left[\frac{1}{\hat{\alpha}\mu nb}\sum_{\alpha=1}^n(g_0^{(\alpha)} - g_y^{(\alpha)})\right]^2.
\tag{38}
$$

Notice that (38) is a convenient relationship between the total dislocation density ρ_T and the hardness $g_0^{(\alpha)}$ averaged over n potential slip systems at reference temperature θ_0. The value of parameter $\hat{\alpha}$ was chosen upon consideration of published data on the dislocation line density (Argon and Maloof, 1966). It should be noted that since the experimental data we used to justify our choice of $\hat{\alpha}$ suffers from an acknowledged lack of precision (Argon and Maloof, 1966), our variable ρ_T should be viewed as a qualitative, yet physically-based, measure useful for comparing the relative degree of strain hardening accumulated in regions of W and matrix phases. Furthermore, since the parameter $\hat{\alpha}$ was chosen from calibration of ρ_T with experimental dislocation density measurements (see Clayton, 2005), the variable ρ_T implicitly enters the energy balance through the presence of $\hat{\alpha}$ in Eq. (37).

Caution must be taken when selecting a value of κ in order to ensure satisfaction of the reduced dissipation inequality (15). If data revealing evolution of β is available from physical experiments (Hodowany et al., 2000; Rosakis et al., 2000), then Eq. (37) can be inverted to select an appropriate value of κ. Vice-versa, if κ is known, then instantaneous values of β can be predicted via (37). From (20) and (37) we see that $\beta \to 1$ as $\kappa \to 0$, meaning no energy of cold working is stored in the lattice when $\kappa = 0$. Subhash et al. (1994) deduced from infrared temperature measurements that β approached unity in high-rate

(i.e., Kolsky bar) compression tests on pure W polycrystals, while Zhou et al. (1994); Zhou (1998) invoked $\beta = 0.90$ for binder and pure W phases in dynamic finite element calculations. Notice that values of β depend strongly upon the form of the rate equations for the slip resistances $g_0^{(\alpha)}$, the latter which, upon consideration of (38), can be interpreted as evolution laws for the dislocation density. Additional detail could be injected into (20) to reflect complex mechanisms of energy storage, but more experimental data are needed to justify a more advanced treatment.

3. Fracture modeling

Consistent with experimental observations of fracture in tungsten alloys (Zamora et al., 1992; Weerasooriya et al., 1994; O'Donnell and Woodward, 2000; Woodward and O'Donnell, 2000; Weerasooriya, 2003), in our framework new surfaces may be created at interfaces between grains of like or different phases, i.e. along W–W grain boundaries and W–matrix boundaries. Intragranular cleavage and separation at matrix–matrix grain boundaries are not represented, as these phenomena were observed less frequently in the aforementioned high-rate tests (Weerasooriya et al., 1994; Weerasooriya, 2003) and in the room temperature, quasi-static experiments of Woodward and O'Donnell (2000). We invoke the dynamic finite element approach (see e.g. Ortiz and Pandolfi, 1999, for theoretical underpinnings), with new fracture surfaces emerging at interfaces between continuum elements when the traction resolved on the potential initiation site exceeds the intrinsic strength of the interface (here, a temperature-dependent material parameter). Hence, fracture initiates when one of the following local stress-based criteria is attained:

$$\hat{s} = \hat{s}_0 + \hat{s}_1(\theta - \theta_0), \quad \hat{\tau} = \hat{\tau}_0 + \hat{\tau}_1(\theta - \theta_0), \tag{39}$$

where $\hat{s}$ and $\hat{\tau}$ are the resolved normal traction and shear traction on the interfacial surface, measured per unit reference configuration area, and $\hat{s}_0$ and $\hat{\tau}_0$ are material parameters specifying the normal and tangential (i.e., mode I and mode II) fracture strengths of the interface at reference temperature θ_0. Linearly temperature-dependent initiation strengths—capturing ductile–brittle transitions, for example—are specified by prescribing nonzero values of $\hat{s}_1$ and $\hat{\tau}_1$ (dimensions of stress/temperature), and various mixed-mode initiation criteria are readily enforced by changing the ratio $\hat{s}_0/\hat{\tau}_0$. In the finite element implementation, duplicate nodes are generated along all potential fracture surfaces during the meshing stage. Initially coincident nodes share the same velocity and temperature histories until either of conditions (39) is reached.

The response of the degraded material at interfaces following initiation is specified by the following coupled irreversible traction–displacement laws (see e.g. Camacho and Ortiz, 1996):

$$\begin{aligned}
\hat{s} &= (\hat{s}_0 + \hat{s}_1(\theta - \theta_0))\left(1 - \frac{\delta_n}{\delta_c}\right), \quad \text{(loading)} \\
\hat{s} &= (\hat{s}_0 + \hat{s}_1(\theta - \theta_0))\left(1 - \frac{\delta_{n1}}{\delta_c}\right)\frac{\delta_n}{\delta_{n1}}, \quad \text{(unloading)}
\end{aligned} \tag{40}$$

$$\begin{aligned}
\hat{\tau} &= (\hat{\tau}_0 + \hat{\tau}_1(\theta - \theta_0))\left(1 - \frac{|\delta_t|}{\delta_c}\right)\left(1 - \frac{\langle\delta_n\rangle}{\delta_c}\right)\text{sgn}(\delta_t), \quad \text{(loading)} \\
\hat{\tau} &= (\hat{\tau}_0 + \hat{\tau}_1(\theta - \theta_0))\left(1 - \frac{|\delta_{t1}|}{\delta_c}\right)\left(1 - \frac{\langle\delta_n\rangle}{\delta_c}\right)\frac{\delta_t}{|\delta_{t1}|}, \quad \text{(unloading)}
\end{aligned} \tag{41}$$

with δ_n and δ_t the normal and tangential crack opening displacements, δ_{n1} and δ_{t1} the maximal values of δ_n and δ_t achieved during the loading history, and δ_c a material parameter describing the separation distance beyond which the cohesive interface no longer supports traction (i.e. complete separation). The Macaulay bracket is written $\langle\rangle$, satisfying $\langle x\rangle = x \; \forall x \geqslant 0$ and $\langle x\rangle = 0 \; \forall x < 0$. As shown in Fig. 2(a) for pure tension
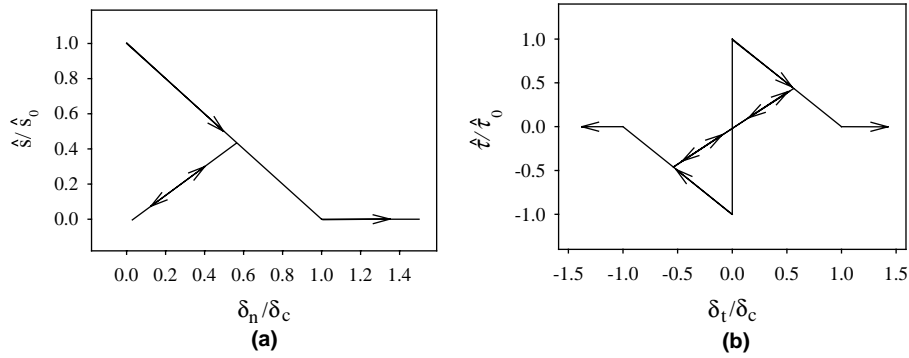
Fig. 2. Isothermal cohesive laws for pure tension (a) and pure shear (b).

and Fig. 2(b) for pure shear, unloading (reloading) occurs linearly to (from) the origin in traction–displacement space. Also prior to attainment of either of criteria (39), heat conduction proceeds as usual. Upon initiation of damage and subsequent separation, however, we enforce the null flux conditions $\nabla_x \theta \cdot \mathbf{n} = 0$, with $\mathbf{n}$ the outward normal to the newly-created fracture surface.

4. Simulations and results

The constitutive models presented in Sections 2 and 3 for bulk and interfacial responses, respectively, were implemented within the EPIC Lagrangian finite element solver (Johnson et al., 1997, 2001; Schoenfeld, 1998). In this approach, the equations of motion are integrated directly and explicitly (see for example Belytschko et al. (1976)). The deformation gradient is updated within each integration point as

$$\mathbf{f}_{t+\Delta t} = \exp(\mathbf{l}\Delta t)\mathbf{f}_t, \tag{42}$$

where $\mathbf{l} = \dot{\mathbf{f}}\mathbf{f}^{-1}$ is the velocity gradient that is assumed constant over the time interval $(t, t + \Delta t)$. The constitutive update proceeds at each integration point via the methodology outlined in Section 2.5. Contributions to the energy balance (19) from plastic dissipation, lattice defects, and thermoelastic coupling are calculated, and then the temperature field is updated explicitly, following the procedure of Johnson (1981). Possible contributions from cohesive elements to global mechanical and thermal force vectors are then calculated prior to the enforcement of external boundary conditions and initiation of the integration step for the deformation field of the next cycle. The stable time increment for each cycle is chosen as a small fraction of the time needed for a longitudinal elastic stress wave to traverse the smallest element in the mesh. A more detailed description of the explicit finite element implementation is given in Appendix A.

Two-dimensional calculations were conducted, with microstructures for meshing obtained from cross-sectional samples of a kinetic energy (KE) rod of the WHA material. Fields-of-view from two different microstructures were considered, as shown in Figs. 3 and 4, each a square window of size $L = 150 \, \mu m$. As a result of processing, W grains in the longitudinal section are elongated in a preferred direction relative to those in the transverse section, with grains in the latter appearing nearly equiaxed. Lattice orientations used as initial conditions in some simulations were obtained from Electron BackScatter Diffraction (EBSD) techniques (Humphreys, 2001). In Figs. 3(b) and 4(b), various colors indicate orientations of normal vectors to the crystallographic planes exposed at the surface (for clarity, only the W phase is shown here). The meshes consist of constant strain triangular elements, generated with the PPM2OOF software (Langer et al., 2003), featuring algorithms for selective grid refinement along material interfaces. The mesh of Fig. 3(c) features 52 distinct W grains, a volume fraction of 82.1% pure W, 16999 standard 3-node bulk
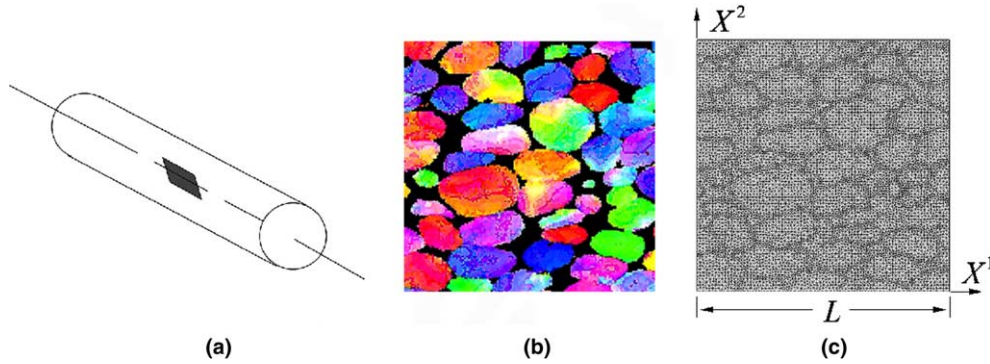
Fig. 3. Longitudinal section: (a) penetrator, (b) lattice orientation map, (c) FE mesh.
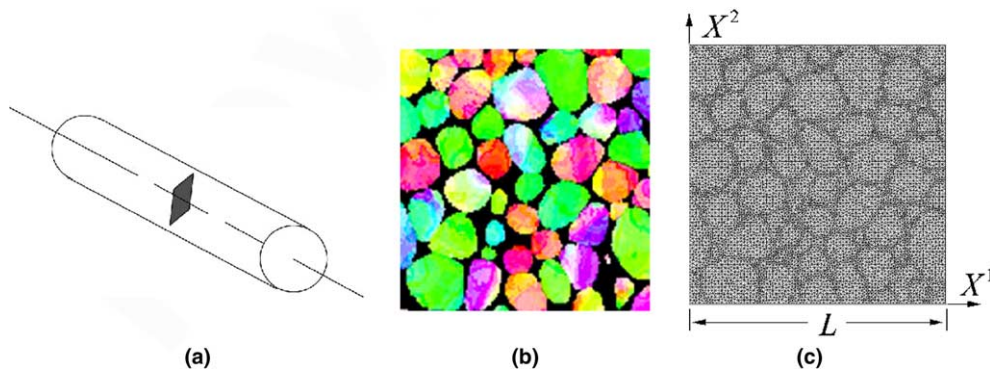

Fig. 4. Transverse section: (a) penetrator, (b) lattice orientation map, (c) FE mesh.

elements, and up to 1879 4-node cohesive elements inserted along grain and phase boundaries. The grid shown in Fig. 4(c) features 51 W grains, 83.9% pure W, 16834 bulk elements, and up to 2028 cohesive elements.

The simulations reported here describe the behavior of the material under impulsive compression loading, similar to conditions that would occur in high velocity plate impact tests (Dandekar and Weisgerber, 1999). Our intention is to track the effects of the bulk microstructural and interfacial properties on the local thermomechanical response history, effects which are not easily deduced from macroscopic physical experiments alone. Via appropriate choice of boundary conditions, we are able to create a situation in which the material spalls as a result of wave reflection, a setting in which we can compare the fracture behavior with other spall experiments of the WHA material reported in the literature (Baoping et al., 1994; Dandekar and Weisgerber, 1999) and parametrically investigate the effects of local interfacial fracture properties on the response (Espinosa and Zavattieri, 2003a,b).

The following boundary and initial conditions were specified. Analyses were plane strain in the $x^1 - x^2$ plane, in essence representing columnar polycrystals extended infinitely in the out-of-plane direction. However, out-of-plane elastic and plastic deformations were permitted (i.e., the 3D material models discussed in Section 2 were employed, with the full complement of slip systems enabling out-of-plane lattice rotations), so long as the total deformation field remained planar. We denote the lower and upper edges of the domain by $X^2 = 0$ and $X^2 = L$, respectively. And let the left and right edges be denoted by $X^1 = 0$ and $X^1 = L$, respectively. The velocity initial and boundary conditions are listed as

$$\dot{x}^1 = (250 \text{ m/s})(t/10^{-9} \text{ s}) \begin{cases} \text{for } 0 \leqslant t \leqslant 10^{-9} \text{ s} \\ \text{along } X^1 = 0 \end{cases}$$

$$\dot{x}^1 = 250 \text{ m/s} \begin{cases} \text{for } 10^{-9}\text{s} \leqslant t \leqslant 10^{-8} \text{ s} \\ \text{along } X^1 = 0 \end{cases}$$

$$\dot{x}^1 = (250 \text{ m/s})([1.1(10^{-8}) \text{ s} - t]/10^{-9} \text{ s}) \begin{cases} \text{for } 10^{-8} \text{ s} \leqslant t \leqslant 1.1(10^{-8}) \text{ s} \\ \text{along } X^1 = 0 \end{cases} \qquad (43)$$

$$\dot{x}^1 = 0 \begin{cases} \text{for } t \geqslant 1.1(10^{-8}) \text{ s} \\ \text{along } X^1 = 0. \end{cases}$$

Conditions (43) result in a rightward-moving compressive pulse of duration 9 ns. Additionally, boundaries along $X^2 = 0$ and $X^2 = L$ were free of shear stress but fixed in the x^2-direction, thus establishing uniaxial strain conditions similar to those that would be encountered by a small volume element of the crystalline material embedded within the target specimen of a plate impact test (see e.g. Meyers, 1994; Becker, 2004):

$$\begin{matrix} t^1 = \sigma^{12} n_2 = 0 \\ \dot{x}^2 = 0 \end{matrix} \text{along} \begin{cases} X^2 = 0 \\ X^2 = L. \end{cases} \qquad (44)$$

The right-hand side of the mesh was traction free, i.e. $\sigma^{ij} n_j = 0$ along $X^1 = L$ for $t \geqslant 0$. Null heat flux boundary conditions were enforced as

$$\nabla_x \theta \cdot \mathbf{n} = 0 \text{ along} \begin{cases} X^1 = 0 \\ X^1 = L \\ X^2 = 0 \\ X^2 = L, \end{cases} \qquad (45)$$

with $\mathbf{n}$ the outward normal vector in the spatial frame, and an initial temperature $\theta_0 = 300$ K was specified uniformly throughout the domain.

Results from nine distinct compression simulations, denoted as simulations 1–9 in Table 3, are reported here. Microstructures and initial lattice orientations are labeled in columns 2 and 3 of Table 3. Simulations 1–3 and 6–9 invoke as initial conditions the experimentally-obtained crystallographic textures corresponding to Figs. 3(b) and 4(b), while simulations 4 and 5 feature purely random initial textures for the W grains and uniform orientations for the matrix phase. Interfacial fracture properties were also varied among simulations, as indicated in columns 4–6. For simulations in which fractures were permitted, values of

Table 3
Simulations

Simulation	Microstructure	Lattice orientation	$\hat{s}_0$ (GPa)	$\hat{\tau}_0$ (GPa)	$\hat{s}_1 = \hat{\tau}_1$ (GPa/K)
1	Longitudinal	Experimental 1	2.0	∞	0
2	Longitudinal	Experimental 1	2.0	4.0	0
3	Transverse	Experimental 2	2.0	∞	0
4	Longitudinal	Random 1	2.0	∞	0
5	Transverse	Random 2	2.0	∞	0
6	Longitudinal	Experimental 1	2.0	∞	0.01
7	Transverse	Experimental 2	2.0	∞	0.01
8	Longitudinal	Experimental 1	∞	∞	0
9	Transverse	Experimental 2	2.0	2.0	0

$\hat{s}_0 = 2.0$ GPa were nominally assigned, in order to roughly match peak stress levels reported in experimental high-rate macroscopic data of Weerasooriya (2003). Dandekar and Weisgerber (1999) estimated from plate impact experiments the spall threshold stress of WHA to lie between 1.7 and 2.0 GPa. Stochastic variations in strength and toughness among interfaces are expected (Woodward and O'Donnell, 2000); though these aspects are not addressed in the present work, such variations could be readily implemented within a cohesive finite element framework such as ours (cf. Zhou and Molinari, 2004). As indicated in column 5, mixed-mode initiation criteria were investigated in several cases by prescribing various values of the initiation strength $\hat{\tau}_0$. For simulations in which shear stress-induced initiation was prohibited (i.e., $\hat{\tau}_0$ of ∞), the value of $\hat{\tau}_0$ in (41) was set equal to $\hat{s}_0$ immediately after the normal stress initiation criterion was achieved, in order to avoid infinite internal reaction forces due to shearing resistance. The choice of infinite initial shear strength is an idealization motivated by Kolsky bar experiments (Weerasooriya and Beaulieu, 1993; Weerasooriya and Moy, 1998; Weerasooriya, 2003) that indicate a tendency for mode I fracture to occur readily relative to modes II and III in the WHA material system. Thermally-dependent fracture strengths were investigated in simulations 6 and 7, in which we allowed the fracture strengths to increase linearly with increasing temperature, in association with the brittle-to-ductile transition in tungsten. Such increase is motivated by the experimental observation of reduced frequency of intergranular fracture events at higher ambient temperatures (O'Donnell and Woodward, 2000) with our designation of a linear dependency of strength on temperature, and particular value of $\hat{s}_1$, following from experimental data reported by Bjerke and Edmanson (2004). All fractures were prohibited in simulation 8, an illustrative scenario designed for comparison of results with the other cases.

We prescribed a uniform value of $\delta_c = 1.0$ µm for the critical separation distance in the cohesive laws of Eqs. (40) and (41), a single value deemed best to represent the effective fracture properties of the WHA material system at the length scale resolved by the numerical discretization (i.e., at the scale of individual grains and their interfaces). Because these tungsten alloys are highly heterogeneous, with fracture behavior dictated by microstructural features such as interfacial strengths and grain contiguity and influenced by large-scale yielding (i.e., finite plastic zones), difficulties arise in obtaining consistent measurements of the macroscopic fracture toughness, with values of $25 \leqslant K_{Ic} \leqslant 234$ MPa$\sqrt{m}$ reported in the literature (Zamora et al., 1992). Furthermore, the microscopic fracture toughness of local interfaces is thought to be smaller in magnitude than that of the homogenized material, as recovered uniaxial test specimens reveal numerous microcracks that do not propagate to cause rupture (Woodward and O'Donnell, 2000). Assuming that the material behaves linear-elastically and neglecting plastic dissipation which may dominate energy release in the cohesive zone (Rice and Wang, 1989), Woodward and O'Donnell (2000) calculated a static plane strain fracture toughness range of $3.4 \leqslant K_{Ic} \leqslant 7.6$ MPa$\sqrt{m}$ for microcracking along interfaces within a WHA. The mode I fracture energy corresponding to $\delta_c = 1.0$ µm and $\hat{s}_0 = 2.0$ GPa is $G_c \equiv (1/2)\hat{s}_0\delta_c = 1.0$ kJ, which, upon assuming for illustrative purposes only, an isotropic linear-elastic stress–strain response for the composite microstructure with an effective elastic modulus of $E = 366$ GPa and a Poisson's ratio of $v = 0.29$ (Dandekar and Weisgerber, 1999), results in a fracture toughness value of $K_{Ic} = \sqrt{G_c E/(1-v^2)} = 20$ MPa$\sqrt{m}$, thought here to be a suitable compromise among the ranges reported in the literature. Note also that our value of δ_c is slightly larger than but of the same order of magnitude of the characteristic length of a typical bulk finite element within the mesh, which we found of adequate resolution to facilitate stable, converged solutions. Cohesive elements were deemed small enough to resolve the process zone, the length of which may be liberally estimated assuming a linear elastic bulk response in the material (Rice, 1968; Espinosa and Zavattieri, 2003b). Specifically, for the present set of material parameters, this mesh refinement criteria was satisfied as follows:

$$d_{cz} = \frac{\pi}{2} \frac{E}{(1-v^2)} \frac{G_c}{\hat{s}_0^2} = 157 \text{ µm} \gg h \approx O(1 \text{ µm}), \tag{46}$$

where d_{cz} is the cohesive zone length and h is the typical element dimension, here on the order of 1 µm.

It should be noted that the spall response of the alloy is highly sensitive to heat treatment. Dandekar and Weisgerber (1999) reported a spall strength of 1.9 ± 0.4 GPa for a swaged WHA, and a spall strength of $\lesssim 1.0$ GPa for an annealed WHA. The constitutive model parameters used for the present set of simulations correspond to the former (swaged) material.

Fig. 5 shows the propagation and reflection of the pressure wave, and the subsequent spall fracture, of the material aggregate of simulation 1. The behavior depicted in Fig. 5 is qualitatively representative of all cases listed in Table 3, except for simulation 8, in which fracture was prohibited, and simulation 9 ($\hat{\tau}_0 = 2.0$ GPa), in which fracture occurred prematurely due to resolved shear stresses associated with the applied compressive wave. Notice how the pressure pulse exhibits modest heterogeneity due to variable properties of the underlying microstructure. By $t = 35$ ns (Fig. 5(d)), the compressive wave front has reached the free surface $X^1 = L$, and tensile hydrostatic stresses ($p < 0$) appear by $t = 40$ ns, resulting in spallation in the bulk of the sample (Fig. 5(f) and Fig. 5(g)). Tensile pressures also arise on the left side of the sample (i.e., near $X^1 = 0$) in the wake of the pressure pulse, due to the fixed boundary condition (43) applied for $t \geqslant 11$ ns, resulting in damage initiation at several locations towards this edge. Regions of relatively high or low pressure do not favor any one phase of the microstructure.

Field variable contours for simulation 1 are shown in Fig. 6, prior to the occurrence of spall fracture, at a simulation time of $t = 20$ ns. The effective deviatoric stress shown in Fig. 6(a) is defined as

$$\sigma_e \equiv \sqrt{3/2(\boldsymbol{\sigma} - p\mathbf{1}) : (\boldsymbol{\sigma} - p\mathbf{1})}. \tag{47}$$

We notice that the distribution of effective stress σ_e is relatively heterogeneous in the wake of the applied pressure pulse, in contrast to the hydrostatic pressure shown previously in Figs. 5(c) and (d), for example. Furthermore, residual deviatoric stresses remain throughout the deformed region of the mesh in Fig. 6(a), a result of incompatible residual elastic deformation due to the mismatch in thermomechanical properties in different grains and phases of the microstructure. Notice that deviatoric stresses tend to concentrate within the stiffer W grains as opposed to the more ductile matrix phase. Effective plastic strains are shown in Fig. 6(b), where

$$\varepsilon_p \equiv \int \sqrt{(2/3)\mathbf{d}^p : \mathbf{d}^p} \mathrm{d}t, \tag{48}$$

with $2\mathbf{d}^p \equiv \mathbf{l}^p + \mathbf{l}^{p\mathrm{T}}$ the rate of plastic stretching referred to the spatial frame. Fig. 6(c) shows the dislocation density ρ_T introduced in Eq. (25), a parameter which correlates strongly with the plastic strain of Fig. 6(b). Recall that our variable ρ_T represents the cumulative increase in shear strength at reference temperature θ_0 averaged over all slip systems, and does not account for increased dislocation mobility that would normally accompany thermal softening. From Figs. 6(b) and (c), respectively, we see that plastic strain and dislocation accumulation concentrate more intensely in regions of the more ductile matrix phase of the WHA under uniaxial high-strain rate compression. Plastic strain magnitudes within interior regions of the mesh frequently exceed $\varepsilon_p = 0.20$, even though the total net strain of the sample remains virtually negligible at the given time instant of the simulation. Baoping et al. (1994) measured a tendency for microhardness of the binder phase to increase much more intensely with increasing shock pressure than the microhardness of the pure W grains. Dislocation accumulation was also much more pronounced in the matrix phase relative to the pure W phase in the shock compression experiments of Baoping et al. (1994), in agreement with results of our simulations. In Fig. 6(d), we see that high temperature regions occur both in the W grains and in the matrix binder in the wake of the compressive shockwave. Notice also in Fig. 6(d) how the temperature rise is greatest towards the left edge of the sample, where the hydrostatic stress state is generally tensile, and at the lateral boundaries. Locally, temperature rises frequently exceed several hundred Kelvin in our simulations. Baoping et al. (1994) reported local temperature increases in excess of 1000 K in a W heavy alloy, albeit shocked at much larger average pressures (in excess of 30 GPa) than those imposed in the present simulations. From Fig. 6(e), we see that the fraction of plastic dissipation converted to heat energy, β of
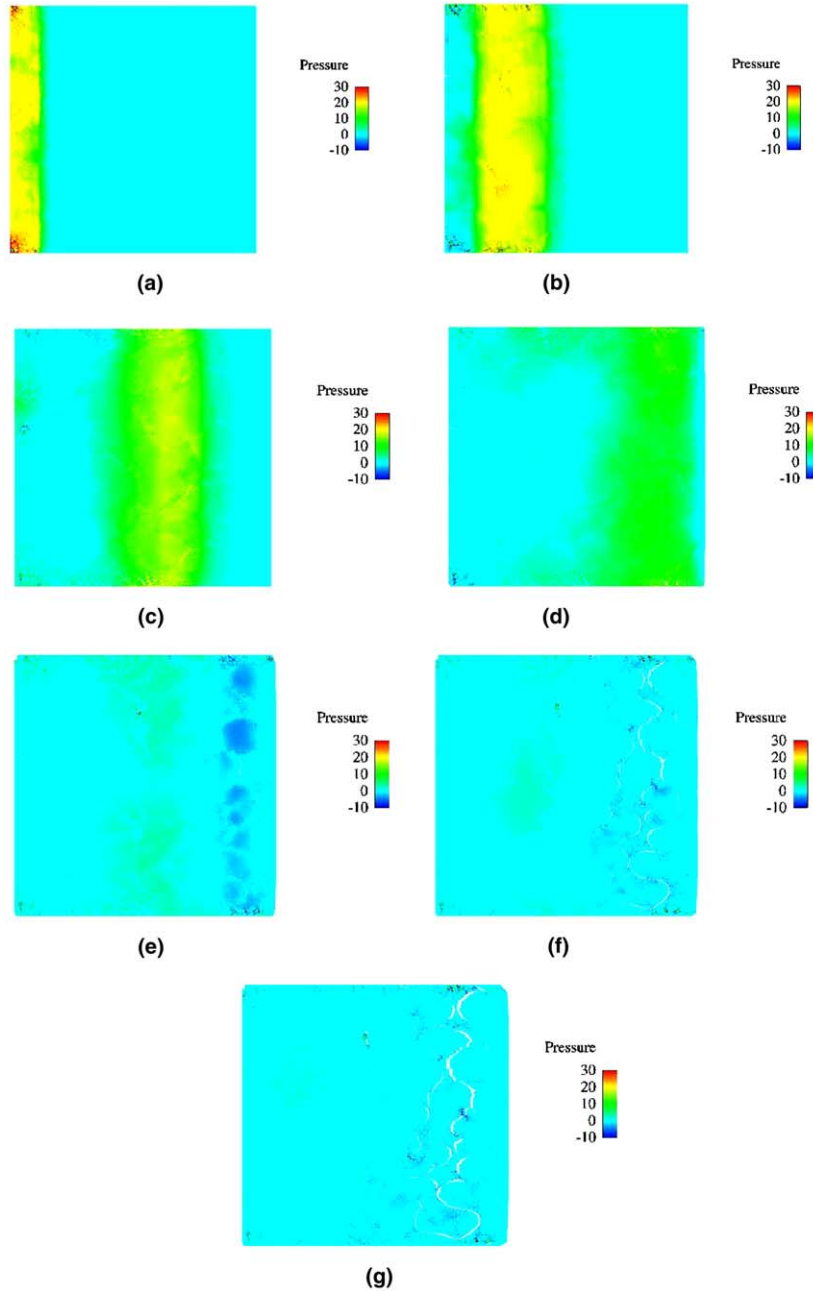
Fig. 5. Hydrostatic pressure p (GPa) for simulation 1, at (a) $t = 5$ ns, (b) $t = 15$ ns, (c) $t = 25$ ns, (d) $t = 35$ ns, (e) $t = 40$ ns, (f) $t = 45$ ns, (g) $t = 50$ ns.

Eqs. (30) and (37), is of generally lower value in the pure W regions than in the matrix regions, indicating a faster instantaneous rate of strain hardening in the former, at $t = 20$ ns. However, values of β (<0.90) tend to follow a gradient from compressed to stretched regions, with $\beta \rightarrow 1.0$ at the front of the compressive
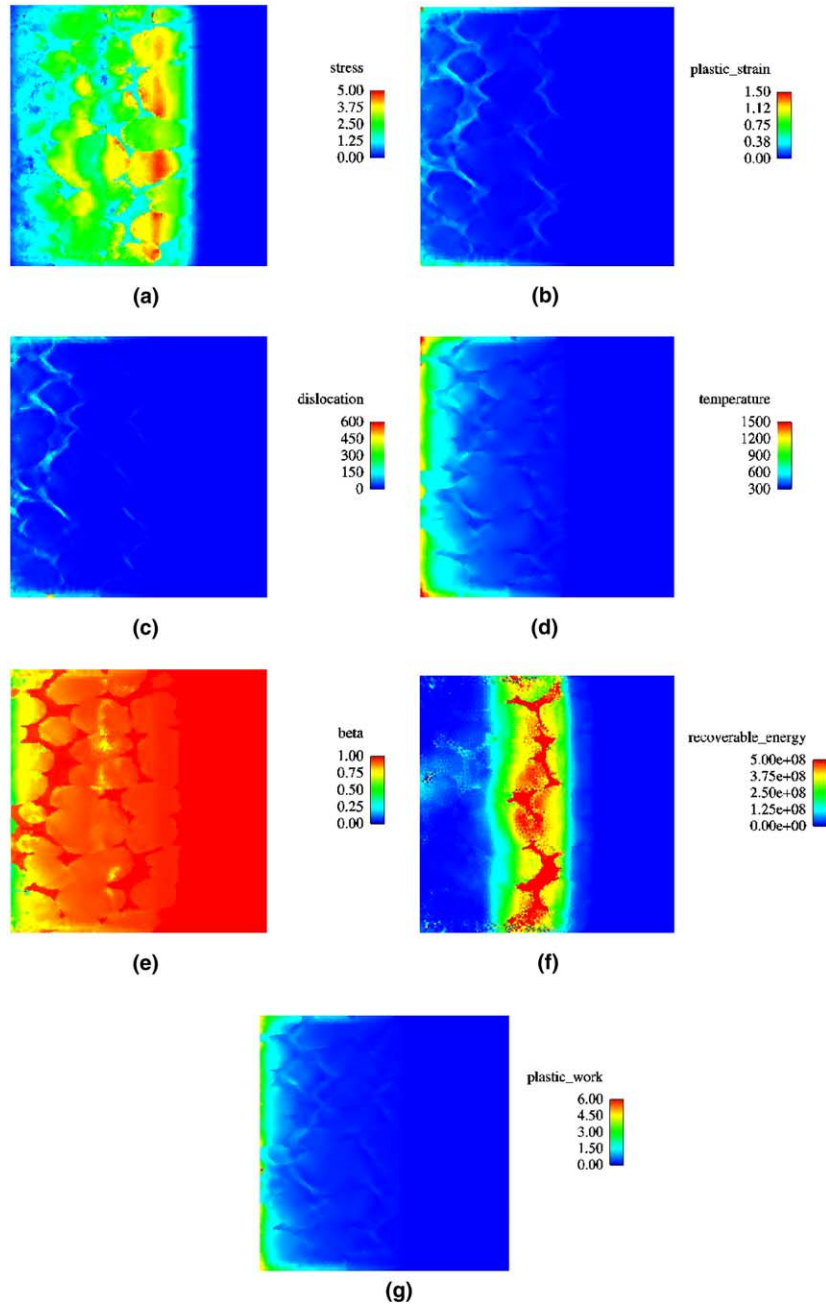
Fig. 6. Contours of field variables for simulation 1 at $t = 20$ ns: (a) effective stress σ_e (GPa), (b) effective plastic strain ε_p, (c) dislocation density ρ_T ($\times 10^{-7}$/cm^2), (d) temperature θ (K), (e) heat dissipation parameter β, (f) recoverable elastic energy density w_e (J/m^3), (g) cumulative plastic work w_p (J/m^3).

pulse. Fig. 6(f) depicts the instantaneous recoverable elastic energy per unit current configuration volume, i.e.,

$$w_e \equiv \left(\frac{1}{2} K_0 \vartheta^2 - \frac{1}{3} K_1 \vartheta^3 + \mu \mathbf{e}^{e'} : \mathbf{e}^{e'} \right) j^{e-1}, \tag{49}$$

large values of which clearly coincide with high pressure regions of the matrix phase, which tends to exhibit relatively larger (in magnitude) compressive deformation ϑ than regions of the pure W phase, a result of the smaller effective bulk modulus of the former. The cumulative plastic work per unit current volume, defined by

$$w_p \equiv \int \left(\sum_{\alpha=1}^n \tau^{(\alpha)} \dot{\gamma}^{(\alpha)} \right) \mathrm{d}t, \tag{50}$$

is shown in Fig. 6(g), with relatively large magnitudes naturally occurring in regions exhibiting large values of temperature rise (Fig. 6(d)). Comparing Figs. 6(f) and (g), notice that the ratio of *recoverable* elastic energy to plastic work, $w^e/w^p \gg 1$, in general. This ratio is not to be confused with the quantity $1 - \beta$, which measures the ratio of the *residual* lattice energy storage rate to the rate of plastic working and generally exhibits values less than unity. Also, from Figs. 6(a)–(g), we observe how the rate- and history-dependent thermoplastic response generally lags the instantaneous elastic response (i.e., pressure and deviatoric stress waves) at the shock front.

Average pressures $\bar{p} \equiv V^{-1} \int p \, \mathrm{d}V$ and temperatures $\bar{\theta} \equiv V^{-1} \int \theta \, \mathrm{d}V$ are shown in Figs. 7(a) and (b), respectively, for simulations labeled 1–8 in Table 3. Here V is the total reference volume of the polycrystalline aggregate. As noted previously, fracture occurred prematurely in simulation 9, a result of resolved shear stresses associated with the applied compressive pulse exceeding the prescribed relatively low value of shear strength of cohesive interfaces, $\hat{\tau}_0 = 2.0$ GPa. For simulation 9 the data are not shown, as local instances of excessive element distortion followed the premature fracture, necessitating early termination of the simulation around $t \approx 20$ ns. Average pressure profiles in Fig. 7(a) are very similar for all eight cases prior to reflection of the applied compression pulse at $X = L$, for $t < 35$ ns. Peak pressures on the order of 6.0 GPa occur at the conclusion of application of the compressive pulse at $t = 11$ ns; subsequently, the average pressures decrease with time, in some cases reaching negative values (tension) upon wave reflection at $t \approx 40$ ns, then increasing again with time as stress waves interact within the bulk material and at the boundaries of the domain. Damage relaxes the reflected tensile stresses in simulations 1–7, while simulation eight supports greater tensile stresses (peak of $\bar{p} = -4.62$ GPa at $t = 66$ ns) since no fracture is permitted. In simulations 6 and 7, the onset of fracture is delayed due to the imposed thermal strengthening criterion at interfaces, thus explaining the larger peak average tensile stresses supported relative to simulation cases 1–5 for $t > 50$ ns. Average temperature increases on the order of 400 K at $t = 100$ ns are apparent in Fig. 7(b), attributed to heterogeneous local plasticity and commensurate inelastic dissipation under nearly adiabatic
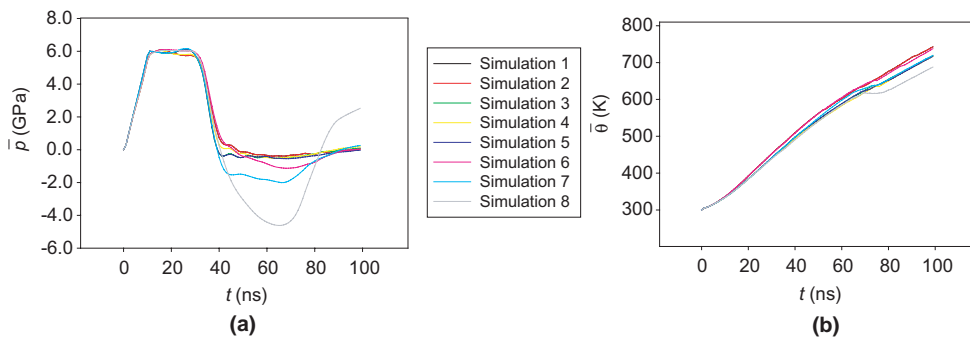

Fig. 7. Volume-averaged field variables versus time t: (a) pressure $\bar{p}$, (b) temperature $\bar{\theta}$.

conditions. Baoping et al. (1994) reported that temperature changes in excess of 1000 K are expected in tungsten alloys subjected to shock pressures in excess of 20 GPa. Notice how the rate (slope) of temperature increase decreases slightly with time, as the average stress state (and corresponding plastic stress power) relaxes. Volume-averaged values of the dissipation fraction β of Eqs. (30) and (37) were found to decrease steadily from unity to approximately 0.70 in each simulation, also contributing to the slowing rate of temperature rise at later solution times.

Fig. 8 shows the total averaged free surface velocity histories $\bar{\dot{x}}^1$ for simulations 1–8, given by the line integral

$$\bar{\dot{x}}^1 \equiv \int_0^{150\ \mu m} \dot{x}^1|_{X^1=L}\, dX^2 \bigg/ \int_0^{150\ \mu m} dX^2, \tag{51}$$

where the local velocity $\dot{x}^1$ in the integrand of Eq. (51) is evaluated along the right (free) surface $X^1 = L$. This information corresponds to what one would typically record in a plate impact experiment with a velocity interferometer system (Barker and Hollenbach, 1972). In general, comparing Figs. 7(a) and 8, we see that the greater the intensity of damage within the polycrystalline aggregate, the smaller the tensile stress and the greater the average free surface velocity for $50 \leqslant t \leqslant 80$ ns, corresponding to the separation of more (spalled) material from the fixed leftward portion of the sample. Maximum average velocities attained around $t = 36$ ns are of comparable magnitudes among some damage simulations (cases 5 and 7) and the damage-free simulation (case 8). For simulation 8, average velocities oscillate about zero for $t \geqslant 50$ ns, as the fixed edge boundary condition at the left side of the mesh, along $X^1 = 0$, prevents the polycrystal from undergoing any rigid-body translation. In contrast, for simulations 1–7, upon spallation, ejected fragments of the material are able to continue to propagate away from the bulk of the specimen, leading to a significant positive free surface velocity. However, these ejected fragments do not regain the impact velocity since the pieces are not completely released in the simulations, as the finite value of critical separation distance specified for stress relief in cohesive zones (Fig. 2) is not achieved at all interfaces along the spall plane. Differences in results for simulations 1 and 2 were negligible (in Figs. 7 and 8 as well as in the deformed FE meshes), as the prescribed shear strength of $\hat{\tau}_0 = 4.0$ GPa was too large relative to the tensile strength of the interface ($\hat{s}_0 = 2.0$ GPa) to permit significant shear-stress-initiated fracture. Comparing data for simulations 1 and 4, and 3 and 5, respectively, we notice effects of initial lattice orientation. Differences in predicted velocities due to microstructure are also apparent by comparing data for simulations 1 (or 2) and 3, corresponding, respectively, to experimental longitudinal and transverse microstructural orientations and grain shapes of Figs. 3 and 4. Comparing average free surface velocities for simulations 6 and 7 with those for simulations 1–5, we notice significantly smaller velocities in the former at later solution times
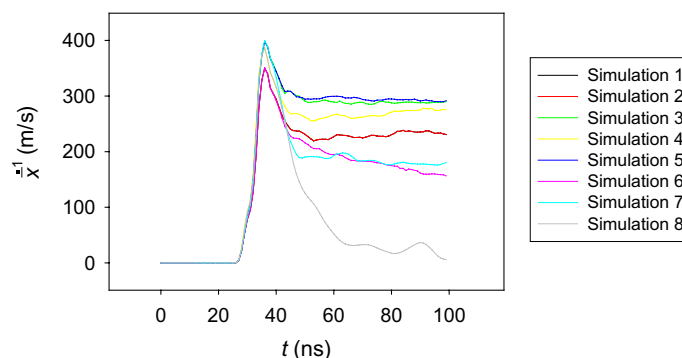

Fig. 8. Spatially-averaged free surface velocity histories.

($t \geqslant 50$ ns). This trend is due to the relative reduction in spall separation associated with increased strength with increasing temperature captured in simulations 6 and 7. Upon consideration of Figs. 7 and 8, we found that interfacial properties (i.e., fracture) apparently exert a more significant influence on the averaged response than do bulk aspects of the microstructure (i.e., grain shapes and orientations). Differences in microcrack patterns were observed in deformed FE meshes to a degree commensurate with trends in the data of Figs. 7 and 8. Although the properties of the bulk microstructure clearly do affect the free surface velocity history (Fig. 8), their effects upon homogenized variables such as pressure and temperature (Fig. 7) are less discernable.

While we could attempt to use the data of Fig. 8 to give some estimation of the bulk spall strength of the WHA, the samples simulated contain too few crystals, and the results too much statistical variability, to make estimations that would be worthwhile to compare quantitatively with experimentally-obtained macroscopic spall strengths (Dandekar and Weisgerber, 1999). Furthermore, the boundary conditions used here are intentionally simpler than those typically encountered in flyer-target plate impact experiments, to allow more straightforward interpretation of the numerical results with regards to variations in material properties.

Fig. 9 gives the time history of the heterogeneity of material (particle) velocity along the traction-free surface $X^1 = L$, defined as the difference between the local value of $\dot{x}^1$ and the average $\bar{\dot{x}}^1$ of Eq. (51):

$$\Delta\dot{x}^1 \equiv \dot{x}^1 - \bar{\dot{x}}^1 = \dot{x}^1 - \int_0^{150\ \mu m} \dot{x}^1|_{X^1=L} dX^2 \Big/ \int_0^{150\ \mu m} dX^2. \tag{52}$$

State-of-the-art methods are presently available to achieve spatial and temporal resolutions of particle velocity, in physical plate impact experiments, at length and time scales comparable to those depicted in Fig. 9 (Vogler et al., 2004). Fig. 9(a) gives data for simulation 1, while Fig. 9(b) gives data for simulation 8. Recall that the former simulation (1) exhibited spall fracture; the latter (8) did not. Grain shapes and initial lattice orientations were identical in each of these two simulations. The relative decreases in velocities near the lateral boundaries at $X^2 = 0$ and $X^2 = L$ are attributed to attenuation of the pressure wave and confinement of the mesh along these edges. For a homogeneous microstructure, the free surface velocity profiles would be symmetric about the centerline $X^2 = L/2 = 75$ μm, and in the absence of lateral boundary effects in such a microstructure, one would have $\Delta\dot{x}^1 = 0$ for all $t \geqslant 0$. Clearly from Fig. 9, neither profile is
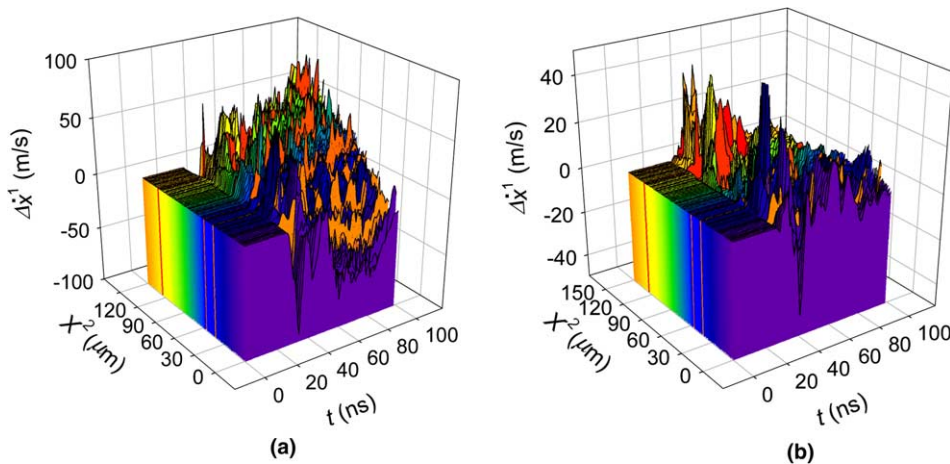

Fig. 9. Free surface velocity perturbation histories for (a) simulation 1 and (b) simulation 8.

symmetric due to the heterogeneous microstructure and corresponding variations in material properties that affect wave propagation through the polycrystal. The profile in Fig. 9(a) is relatively more intense and jagged, spatially and temporally, than that in Fig. 9(b), especially for $t > 40$ ns, because of the heterogeneous distribution of microcracks and fragments formed during spallation in later stages of the former simulation.

5. Conclusions

Continuum crystal plasticity models for a two-phase tungsten heavy alloy have been developed, accounting for finite deformation, plastic anisotropy, large volumetric strain, heat conduction, thermoelastic heating, rate- and temperature-dependent flow stress, and stored internal energy due to lattice defects. A rate independent cohesive zone framework has been presented, capturing effects of temperature and mode mixity on damage initiation and evolution at grain and phase boundaries. Numerical simulations of polycrystalline aggregates of the alloy under shock compression conditions indicate the following trends in material behavior:

- The pure W phase supports higher deviatoric stresses than the more ductile matrix phase.
- The matrix phase accommodates larger inelastic strains and exhibits greater dislocation accumulation associated with strain hardening, relative to the W phase.
- The instantaneous rate of temperature rise and fraction of plastic dissipation converted to heat energy may favor either phase, depending upon the stress state and time instant of the deformation history.
- Grain shapes and initial lattice orientations exert a noticeable influence on the shape and local intensity of propagating and reflected stress waves, even in the absence of fracture.
- Interfacial properties controlling the effects of stress state (e.g. mixed mode fracture criteria) and temperature on microcrack initiation and propagation significantly affect the evolution of spall-induced damage, and hence, the overall spall strength of the material.

The conditions of applicability of the model framework presented and implemented here are now noted. The thermoelasticity framework and associated parameters of Table 1 are thought to be reasonably valid for tungsten subjected to local pressures less than 35 GPa, corresponding to elastic volume changes less than on the order of 10%. Phase changes are not captured, as transitions from BCC to FCC or DHCP (double hexagonal close packed) structures are observed in tungsten at pressures on the order of 65 GPa (cf. Ruoff et al., 1998). Also, the melting temperature of pure W is 3410 K, while that of the matrix is approximately 1750 K (Zhou and Clifton, 1997). Neither material attained its melting point in our simulations. The thermoelasticity model used for the binder phase is linear and isotropic, due to limited availability of experimental data. The framework used for rate-dependent plastic deformation in both phases of the alloy (see also Clayton, 2005) was calibrated to the materials' homogeneous stress–strain responses spanning quasi-static (0.0001/s) to high strain rates (10,000/s), despite the possible manifestation of higher local inelastic strain rates during simulations of wave propagation as occurs in plate impact experiments. The plasticity models may be concretely verified, and modified as necessary, for higher strain rate applications (i.e., in excess of 10,000/s) as reliable experimental data become available. Additional avenues for improving the physical description of WHA behavior in the context of our modeling framework include the following:

- Delineation of the role of crystallographic twinning observed in tungsten crystals subjected to high strain rates and large pressures (cf. Pappu et al., 2001) from that of dislocation glide in the plasticity framework.

- Characterization of non-Schmid effects and slip strength anisotropy on {112} planes as observed in atomistic and experimental studies on pure W (Duesberry and Vitek, 1998).
- Incorporation of a model for cleavage fracture of W grains along known intrinsically weak planes of orientation {100} and {110} and accounting for the thermal dependence of the measured fracture toughness of these planes (Gumbsch et al., 1998).
- Depiction of length scale effects such as grain size influences on strength, hardness and susceptibility to plastic flow instability, as experimentally observed in tungsten during grain refinement (i.e., subgrain formation) commensurate with severe plastic deformation processes (Aleksandrov et al., 2002).

We emphasize that the present work offers an increased understanding of how one may interpret experimental data on shock wave propagation and spall fracture in tungsten alloys with regards to effects of bulk microstructural and interfacial thermomechanical properties. Future studies will involve direct assessments of results from plate impact tests and numerical predictions under comparable boundary conditions. Specifically, comparisons of spatially-resolved particle velocity profiles from experiments (Vogler et al., 2004) and simulations are envisioned.

Acknowledgements

Appendix A

Details of the numerical procedure used for the explicit finite element calculations are outlined here. In the absence of body forces, the global principal of virtual work corresponding to the linear momentum balance in (6) can be written as follows in the spatial frame (see e.g., Zhou and Molinari, 2004):

$$\int_v (\rho \ddot{\mathbf{x}} \cdot \delta \dot{\mathbf{x}}) \mathrm{d}v = -\int_v (\boldsymbol{\sigma} : \delta \mathbf{d}) \mathrm{d}v - \int_{s_i} (\mathbf{t} \cdot [\![\delta \dot{\mathbf{x}}]\!]) \mathrm{d}s_i + \int_{s_e} (\mathbf{t} \cdot \delta \dot{\mathbf{x}}) \mathrm{d}s_e, \tag{A.1}$$

where δ denotes an admissible variation, the spatial deformation rate tensor $2\mathbf{d} \equiv \frac{\partial \dot{\mathbf{x}}}{\partial \mathbf{x}} + \left(\frac{\partial \dot{\mathbf{x}}}{\partial \mathbf{x}}\right)^{\mathrm{T}}$, the traction per unit spatial area $\mathbf{t} = \boldsymbol{\sigma} \cdot \mathbf{n}$, and s_i and s_e denote internal and external surfaces of the current volume v. The jump in virtual velocity across internal (cohesive) surface s_i is written $[\![\delta \dot{\mathbf{x}}]\!]$. The energy balance (19), in global variational form and assuming nonconducting internal surfaces, is written as

$$\int_v (\rho \hat{c} \dot{\theta} \delta \theta) \mathrm{d}v = \int_v (\Phi \delta \theta) \mathrm{d}v - \int_v \left(k \frac{\partial \theta}{\partial \mathbf{x}} \cdot \frac{\partial \delta \theta}{\partial \mathbf{x}}\right) \mathrm{d}v + \int_{s_e} \left(k \frac{\partial \theta}{\partial \mathbf{x}} \cdot \mathbf{n} \delta \theta\right) \mathrm{d}s_e, \tag{A.2}$$

where

$$\Phi \equiv \sum_{\alpha=1}^n \tau^{(\alpha)} \dot{\gamma}^{(\alpha)} - \rho((\partial_\xi \psi) - \theta(\partial_{\theta\xi} \psi)) \dot{\xi} + \rho \theta \partial_{\theta \mathbf{e}^e} \psi : \dot{\mathbf{e}}^e. \tag{A.3}$$

Finite element discretization of (A.1) leads to

$$\mathbf{M}\ddot{\mathbf{X}} = \mathbf{R}^{\mathrm{v}} + \mathbf{R}^{\mathrm{i}} + \mathbf{R}^{\mathrm{e}}, \tag{A.4}$$

where $\mathbf{M}$ is the nodal mass matrix, $\ddot{\mathbf{X}}$ is the vector of nodal accelerations, $\mathbf{R}^{v}$ is the vector of internal forces corresponding to internal stresses and associated with the first term on the right side of (A.1), $\mathbf{R}^{i}$ is due to forces exerted by cohesive tractions associated with the second term on the right-hand side of (A.1), and $\mathbf{R}^{e}$ is the vector of externally-applied forces resulting from third term on the right-hand side of (A.1). Analogously, the finite element equation corresponding to (A.2) can be written as (cf. Zhou, 1998)

$$\widehat{\mathbf{C}}\dot{\boldsymbol{\Xi}} = \boldsymbol{\Phi} + \mathbf{K}\boldsymbol{\Xi}, \tag{A.5}$$

where $\widehat{\mathbf{C}}$ is the nodal heat capacitance matrix, $\boldsymbol{\Xi}$ is the vector of nodal temperatures, $\boldsymbol{\Phi}$ includes the contribution of internal heating from the first term on the right of (A.2), and $\mathbf{K}$ is the matrix of heat conduction.

The solution algorithm proceeds stepwise in time as follows. Recall that displacements and temperatures vary linearly over the 3-node triangular elements used to model the material continuum. Let subscript n denote the iteration number corresponding to the nth time increment in the integration cycle. The acceleration vector is found from (A.4) as

$$\ddot{\mathbf{X}}_{n+1} = \mathbf{M}^{-1}(\mathbf{R}_{n}^{v} + \mathbf{R}_{n}^{i} + \mathbf{R}_{n}^{e}), \tag{A.6}$$

where the right-hand side has been calculated from the solution of the previous cycle, or from the initial conditions for the case of $n = 0$. The nodal velocity and position vectors are next updated sequentially as follows (Johnson et al., 1997):

$$\dot{\mathbf{X}}_{n+1} = \dot{\mathbf{X}}_{n} + \frac{1}{2}(t_{n+1} - t_{n-1})\ddot{\mathbf{X}}_{n+1}, \tag{A.7}$$

$$\mathbf{X}_{n+1} = \mathbf{X}_{n} + (t_{n+1} - t_{n})\dot{\mathbf{X}}_{n+1}. \tag{A.8}$$

Analogously, the temperature field is updated explicitly via

$$\dot{\boldsymbol{\Xi}}_{n+1} = \widehat{\mathbf{C}}_{n}^{-1}(\boldsymbol{\Phi}_{n} + \mathbf{K}_{n}\boldsymbol{\Xi}_{n}), \tag{A.9}$$

$$\boldsymbol{\Xi}_{n+1} = \boldsymbol{\Xi}_{n} + (t_{n+1} - t_{n})\dot{\boldsymbol{\Xi}}_{n+1}, \tag{A.10}$$

where the temperature-dependent capacitance and conductivity matrices have been evaluated during cycle n, as has the thermal force vector $\boldsymbol{\Phi}_{n}$, which in our simulations consists primarily of the contribution to heating from plastic dissipation. Note also that nodal velocities and temperatures of (A.7) and (A.9) are updated consistently with externally imposed velocity and temperature boundary conditions wherever specified. At this stage, local velocity gradients $\mathbf{l}_{n+1}$ are calculated at the integration point (i.e., centroid) of each element, and the deformation gradient $\mathbf{f}_{n+1}$ is found at each integration point from (42), i.e.,

$$\mathbf{f}_{n+1} = \exp(\mathbf{l}_{n+1}(t_{n+1} - t_{n}))\mathbf{f}_{n}. \tag{A.11}$$

Correspondingly the temperature is updated within each element in a manner consistent with Eqs. (29), (31), (A.9), and (A.10):

$$\theta_{n+1} = \theta_{n} + (t_{n+1} - t_{n})\dot{\theta}_{n+1}. \tag{A.12}$$

The thermoelastic–viscoplastic update within each element then proceeds according to the method discussed in Section 2.5; for additional details regarding the numerical algorithm, the reader is referred to McGinty (2001). This constitutive update, which is the most time consuming portion of the calculation, is conducted in parallel over multiple processors. The outcome of the constitutive update is the local stress field $\boldsymbol{\sigma}_{n+1}$, which in turn contributes to $\mathbf{R}_{n+1}^{v}$ to appear in the next iteration of (A.6), as well as the thermal force contribution $\boldsymbol{\Phi}_{n+1}$ to appear in the next iteration of (A.9). We employ an element failure criterion in order to prevent excessively deformed elements from corrupting the solution and interfering the time incre-

mentation scheme to be discussed shortly (i.e., such elements do not enter Eq. (A.15)). Following common practice in dynamic Lagrangian finite element codes (Johnson et al., 2001), elements accumulating a very large magnitude of plastic strain, specifically $\varepsilon_p \geqslant 10.0$, are not permitted to contribute to $\mathbf{R}_{n+1}^v$, $\mathbf{\Phi}_{n+1}$, and $\mathbf{K}_{n+1}$ for the next cycle, and the local constitutive update is subsequently bypassed in these elements. In the present context, this action is justified by the association of very large inelastic deformations with very large temperature increases, resulting in relatively small stresses due to thermal softening (Eq. (24)). Masses and capacitances are conserved in the nodes comprising these elements, however. Recall also that duplicate nodes exist at interfaces between some triangular elements (in our case along grain and phase boundaries) where fractures may occur. At this point in the computation, the normal traction $\hat{s}$ and shear traction $\hat{\tau}$ (per unit reference area) are computed along each potential fracture face as an average of the resolved stresses found from the stress fields of the two elements sharing that face. Criteria (39) are then tested, with the average temperature at the interface used when either of $\hat{s}_1$ or $\hat{\tau}_1$ is nonzero. If neither initiation criterion is achieved at the interface, then nodal pairs at either end that interface are required to maintain the same displacement and temperature values for the next time increment, i.e.,

$$(\ddot{X}_{n+2})|_A = (\ddot{X}_{n+2})|_B = \frac{(R_{n+1}^v + R_{n+1}^i + R_{n+1}^e)|_A + (R_{n+1}^v + R_{n+1}^i + R_{n+1}^e)|_B}{M_A + M_B}, \tag{A.13}$$

$$(\dot{\Theta}_{n+2})|_A = (\dot{\Theta}_{n+2})|_B = \frac{(\Phi_{n+1} + K_{n+1}\Theta_{n+1})|_A + (\Phi_{n+1} + K_{n+1}\Theta_{n+1})|_B}{(\widehat{C}_{n+1})|_A + (\widehat{C}_{n+1})|_B}, \tag{A.14}$$

for pinned coincident nodes with associated quantities labeled by subscripts A and B. When three or more nodes are pinned at an interface junction (e.g., a grain boundary triple point), relations (A.13) and (A.14) are extended in a straightforward manner. On the other hand, if either of fracture initiation criteria (39) is achieved, the nodal pairs sharing the interface are unpinned and free to acquire different positions and temperatures as the solution proceeds. The next term needed for the subsequent solution increment is the force vector $\mathbf{R}_{n+1}^i$, which is now computed from the integrating the traction resulting from displacement jumps across active cohesive surfaces. The traction contributing to $\mathbf{R}_{n+1}^i$ are computed through relations (40) and (41), with displacement jumps calculated in terms of the solution $\mathbf{X}_{n+1}$ from (A.8). Additionally, a restoring force is added to $\mathbf{R}_{n+1}^i$ to prohibit interpenetration of matter when compressive traction is transmitted across initiated (unpinned) cohesive surfaces. Finally, the contribution from external boundary conditions, $\mathbf{R}_{n+1}^e$, is computed. The next integration cycle is then commenced (Eqs. (A.6) and (A.9)), with the new time increment chosen as

$$t_{n+2} - t_{n+1} = \min_{\text{elements}} \left(\frac{\varsigma h}{\sqrt{(\lambda + 2\mu)/\rho}}, \frac{\varsigma \rho \hat{c} h^2}{4k} \right) \Bigg|_{n+1}, \tag{A.15}$$

where $\varsigma < 1$ is a security coefficient, h is the element dimension, the first term in parentheses is the constraint imposed such that stress waves are properly resolved in the continuum elements (λ is Lamé's elastic stiffness constant), and the second term in parentheses ensures stable computations for heat conduction. The stress wave constraint dominated the time incrementation scheme for the computations conducted here as a result of the specified mesh dimensions, boundary conditions, and material properties. When cohesive finite elements are used in dynamic calculations, a very small value of ς is typically required in order to maintain stability. Such small time steps are needed for two reasons: in order to minimize numerical smoothing of stress waves traversing a grid in which duplicate nodes are unpinned yet transmit forces, and in order to ensure very small crack opening displacement perturbations in each iteration such that the cohesive traction–displacement law is adequately resolved (Xu and Needleman, 1994; Espinosa and Zavattieri, 2003a,b; Zhou and Molinari, 2004). In dynamic finite element simulations of cohesive fracture, Xu and Needleman (1994) and Zhou and Molinari (2004) employed criteria (A.15) with reported values of

the security factor ς ranging from ς = 0.01 ∼ 0.1. In the simulations reported here, following a trial-and-error investigation, a conservative value of ς = 0.01 was found to yield consistently converged results.

References

Aleksandrov, I.V., Raab, G.I., Shestakova, L.O., Kil'mametov, A.R., Valiev, R.Z., 2002. Refinement of tungsten microstructure by severe plastic deformation. Phys. Met. Metall. 93, 493–500.

Aravas, N., Kim, K.S., Leckie, F.A., 1990. On the calculations of the stored energy of cold work. J. Eng. Mat. Tech. 112, 465–470.

Argon, A.S., Maloof, S.R., 1966. Plastic deformation of tungsten single crystals at low temperatures. Acta Metall. 14, 1449–1462.

Armstrong, P.J., Frederick, C.O., 1966. A mathematical representation of the multiaxial Bauschinger effect. CEGB Report No. RD/B/N, 731.

Asaro, R.J., 1983. Crystal plasticity. J. Appl. Mech. 50, 921–934.

Asay, J.R., Chhabildas, L.C., Dandekar, D.P., 1980. Shear strength of shock-loaded polycrystalline tungsten. J. Appl. Phys. 51, 4774–4783.

Ashmawi, W.M., Zikry, M.A., 2003. Grain boundary effects and void porosity evolution. Mech. Mater. 35, 537–552.

Bammann, D.J., 2001. A model of crystal plasticity containing a natural length scale. Mat. Sci. Eng. A309–310, 406–410.

Baoping, Z., Chao, Y., Yingming, X., Chunlan, J., 1994. Responsive behaviour of 93 wt.% tungsten alloy under the intense shock loading. In: Zhemin, Z., Quingming, T. (Eds.), Proc. IUTAM Symposium on Impact Dynamics. Peking University Press, Peking, PRC, pp. 283–297.

Barenblatt, G.I., 1959. The formation of equilibrium cracks during brittle fracture: general ideas and hypotheses, axially symmetric cracks. Appl. Math. Mech. 23, 622–636.

Barker, L.M., Hollenbach, R.E., 1972. Laser interferometer for measuring high velocities of any reflecting surface. J. Appl. Phys. 43, 4669–4675.

Becker, R., 2004. Effects of crystal plasticity on materials loaded at high pressures and strain rates. Int. J. Plast. 20, 1983–2006.

Belytschko, T., Chiapetta, R.L., Bartel, H.D., 1976. Efficient large scale non-linear transient analysis by finite elements. Int. J. Numer. Meth. Engng. 10, 579–596.

Bjerke, T.W., Edmanson, W.R., 2004. High rate plastic deformation and failure of tungsten-sintered materials. In: Proceedings of the 10th International Congress for the Society of Experimental Mechanics, June 7–10, Costa Mesa, CA.

Bruchey, W.J., Herring, R.A., Kingman, P.W., Horwath, E.J., 1992. Deformation mechanisms in tungsten single crystals in ballistic impact experiments. In: Asfahnai, R. et al. (Eds.), High Strain Rate Behavior of Refractory Metals and Alloys. TMS, Warrendale, PA.

Bruchey, W.J., Horwath, E.J., Kingman, P.W., 1991. Orientation dependence of deformation and penetration behavior of tungsten single-crystal rods. In: Crowson, A., Chen, E. (Eds.), Tungsten and Tungsten Alloys, Recent Advances. TMS, Warrendale, PA.

Cai, W.D., Li, Y., Dowding, R.J., Mohamed, F.A., Lavernia, E.J., 1995. A review of tungsten-based alloys as kinetic energy penetrator materials. Rev. Particu. Mater. 3, 71–132.

Camacho, G.T., Ortiz, M., 1996. Computational modelling of impact damage in brittle materials. Int. J. Solids Struct. 33, 2899–2938.

Clayton, J.D., 2005. Dynamic plasticity and fracture in high density polycrystals: constitutive modeling and numerical simulation. J. Mech. Phys. Solids 53, 261–301.

Clayton, J.D., Bammann, D.J., McDowell, D.L., 2004. Anholonomic configurations and metric tensors in finite elastoplasticity. Int. J. Nonlinear Mech. 39, 1039–1049.

Coleman, B.D., Noll, W., 1963. The thermodynamics of elastic materials with heat conduction and viscosity. Arch. Rat. Mech. Anal. 13, 167–178.

Cuitiño, A., Ortiz, M., 1992. A material-independent method for extending stress update algorithms from small-strain plasticity to finite plasticity with multiplicative kinematics. Eng. Computations 9, 437–452.

Dandekar, D.P., 1976. Loss of shear strength in polycrystalline tungsten under shock compression. J. Appl. Phys. 47, 4703–4705.

Dandekar, D.P., Weisgerber, W.J., 1999. Shock response of a tungsten heavy alloy. Int. J. Plast. 15, 1291–1309.

Duesberry, M.S., Vitek, V., 1998. Plastic anisotropy in BCC transition metals. Acta Mater. 46, 1481–1492.

Dümmer, T., Lasalvia, J.C., Ravichandran, G., Meyers, M.A., 1998. Effect of strain rate on plastic flow and failure in polycrystalline tungsten. Acta Mater. 46, 6267–6290.

Espinosa, H.D., Zavattieri, P.D., 2003a. A grain level model for the study of failure initiation and evolution in polycrystalline brittle materials. Part I: Theory and numerical implementation. Mech. Mater. 35, 333–364.

Espinosa, H.D., Zavattieri, P.D., 2003b. A grain level model for the study of failure initiation and evolution in polycrystalline brittle materials. Part II: numerical examples. Mech. Mater. 35, 365–394.

Grüneisen, E., 1926. Handbuch der Physik, Vol. 10, Springer, Berlin.

Gumbsch, P., Riedle, J., Hartmaier, A., Fischmeister, H.F., 1998. Controlling factors for the brittle-to-ductile transition in tungsten single crystals. Science 282, 1293–1295.

Hodowany, J., Ravichandran, G., Rosakis, A.J., Rosakis, P., 2000. Partition of plastic work into heat and stored energy in metals. Experim. Mech. 40, 113–123.

Horstemeyer, M.F., McDowell, D.L., McGinty, R.D., 1999. Design of experiments for constitutive model selection: application to polycrystal elastoviscoplasticity. Modelling Simul. Mater. Sci. Eng. 7, 253–273.

Horwath, E.J., 1994. The high strain rate deformation of tungsten single crystals. ARL-TR-620.

Humphreys, F.J., 2001. Grain and subgrain characterisation by electron backscatter diffraction. J. Mat. Sci. 36, 3833–3854.

Hutchinson, J.W., 1976. Bounds and self-consistent estimates for creep of polycrystalline materials. Proc. R. Soc. Lond. A348, 101–127.

Johnson, G.R., 1981. Dynamic analysis of a torsion test specimen including heat conduction and plastic flow. J. Eng. Mater. Tech. 103, 201–206.

Johnson, G.R., Stryk, R.A., Holmquist, T.J., Beissel, S.R., 1997. Numerical algorithms in a Lagrangian hydrocode. WL-TR-1997-7039. Wright Laboratory, Armament Directorate, USA Approved for public release, unlimited distribution.

Johnson, G.R., Stryk, R.A., Beissel, S.R., 2001. User instructions for the 2001 version of the EPIC code. Alliant Techsystems Inc., Hopkins, MN. Distribution authorized to U.S. government agencies and their contractors.

Klopp, R.W., Clifton, R.J., Shawki, T.G., 1985. Pressure-shear impact and the dynamic viscoplastic response of metals. Mech. Mater. 4, 375–385.

Kobytev, V.S., Lazareva, L.I., Popov, L.E., Pudan, L.Y., 1984. Build-up of strain defects and the energetics of plastic strain. Izv. Vys. Uch. Zav., Fiz. 4, 12–16.

Kuhlmann-Wilsdorf, D., 1985. Theory of workhardening, 1934–1984. Metal Trans. 16A, 2091–2108.

Langer, S., Reid, A., Carter, C., Fuller, E., Roosen, A., 2003. PPM2OOF v1.1. Available from <http://www.ctcms.nist.gov/>.

Lee, Y.J., Subhash, G., Ravichandran, G., 1999. Constitutive modeling of textured body-centered-cubic (bcc) polycrystals. Int. J. Plast. 15, 625–645.

Lee, B.J., Vecchio, K.S., Ahzi, S., Schoenfeld, S., 1997. Modeling the mechanical behavior of tantalum. Metals Mater. Trans. A28, 113–122.

Magness, L.S., 1994. High strain rate deformation behaviors of kinetic energy penetrator materials during ballistic impact. Mech. Mater. 17, 147–154.

Marsden, J.E., Hughes, T.J.R., 1983. Mathematical Foundations of Elasticity. Dover, New York.

McGinty, R.D., 2001. Multiscale Representation of Polycrystalline Inelasticity. Ph.D. Thesis, Georgia Institute of Technology.

Meyers, M.A., 1994. Dynamic Behavior of Materials. John Wiley & Sons, New York.

O'Donnell, R.G., Woodward, R.L., 2000. Influence of temperature on the fracture of a W–Ni–Fe alloy. J. Mater. Sci. 35, 4319–4324.

Ortiz, M., Pandolfi, A., 1999. Finite-deformation irreversible cohesive elements for three-dimensional crack-propagation analysis. Int. J. Numer. Meth. Eng. 44, 1267–1282.

Pappu, S., Sen, S., Murr, L.E., Kapoor, D., Magness, L.S., 2001. Deformation twins in oriented, columnar-grained tungsten rod ballistic penetrators. Mat. Sci. Eng. A298, 144–157.

Qiu, X., Huang, Y., Nix, W.D., Hwang, K.C., Gao, H., 2001. Effect of intrinsic lattice resistance in strain gradient plasticity. Acta Mater. 49, 3949–3958.

Rice, J.R., 1968. Mathematical analysis in the mechanics of fracture. In: Liebowitz, H. (Ed.), Fracture, an Advanced Treatise. Academic Press, New York, pp. 191–311.

Rice, J.R., Wang, J.-S., 1989. Embrittlement of interfaces by solute segregation. Mat. Sci. Eng. A107, 23–40.

Rosakis, P., Rosakis, A.J., Ravichandran, G., Hodowany, J., 2000. A thermodynamic internal variable model for the partition of plastic work into heat and stored energy in metals. J. Mech. Phys. Solids, 581–607.

Ruoff, A.L., Rodriguez, C.O., Christensen, N.E., 1998. Elastic moduli of tungsten to 15 Mbar, phase transition at 6.5 Mbar, and rheology to 6 Mbar. Phys. Rev. B 58, 2998–3002.

Schoenfeld, S.E., 1998. Dynamic behaviour of polycrystalline Ta. Int. J. Plast. 14, 871–890.

Schoenfeld, S.E., Benson, D.J., 1997. Modeling penetration mechanisms and ballistic performance in high aspect ratio tungsten single-crystal rods: a crystal plasticity model suitable for impact calculations. In: Atluri, S.N., Yagawa, G. (Eds.), Advances in Computational Engineering Science. Tech Science Press, pp. 1116–1121.

Simo, J.C., Ortiz, M., 1985. A unified approach to finite deformation elastoplastic analysis based on the use of hyperelastic constitutive equations. Comp. Meth. Appl. Mech. Eng. 49, 221–245.

Stevens, J.B., Batra, R.C., 1998. Adiabatic shear bands in the Taylor impact test for a WHA rod. Int. J. Plast. 14, 841–854.

Subhash, G., Lee, Y.J., Ravichandran, G., 1994. Plastic deformation of CVD textured tungsten, part I: constitutive response. Acta Metall. Mater. 42, 319–330.

Svendsen, B., 2002. Continuum thermodynamic models for crystal plasticity including the effects of geometrically-necessary dislocations. J. Mech. Phys. Solids 50, 1297–1329.

Taylor, G.I., 1934. The mechanism of plastic deformation of crystals. Proc. R. Soc. Lond. A145, 362–415.

Taylor, G.I., 1938. Plastic strain in metals. J. Inst. Metals 62, 307.

Taylor, G.I., Quinney, H., 1934. The latent energy remaining in a metal after cold working. Proc. R. Soc. Lond. A143, 307–326.

Vogler, T.J., Reinhart, W.D., Chhabildas, L.C., 2004. Dynamic behavior of boron carbide. J. Appl. Phys. 95, 4173–4183.

Weerasooriya, T., 1998. Deformation behavior of 93W–5Ni–2Fe at different rates of compression loading and temperature. ARL-TR-1719, July 1998.

Weerasooriya, T., 2003. Deformation and failure behavior of a tungsten heavy alloy under tensile loading at different strain rates. Presented at SEM Annual Conference on Experimental Mechanics, Charlotte, NC, USA, June 2–4.

Weerasooriya, T., Beaulieu, P.A., 1993. Effects of strain rate on the deformation and failure behavior of 93W–5Ni–2Fe under shear loading. Mater. Sci. Eng. A172, 71–78.

Weerasooriya, T., Moy, P., 1998. High shear strain-rate behavior of W–Ni–Fe tungsten heavy alloy composites as a function of matrix volume fraction. ARL-TR-1694.

Weerasooriya, T., Moy, P., Dowding, R., 1994. Effect of W–W contiguity on the high shear strain rate behavior of 93W–5Ni–2Fe tungsten heavy alloy. In: Bose, A., Dowding, R. (Eds.), Proceedings of the 2nd International Conference on Tungsten and Refractory Metals, Metal Powder Industries, pp. 401–409.

Wei, Z., Yu, J., Hu, S., Li, Y., 2000. Influence of microstructure on adiabatic shear localization of pre-twisted tungsten heavy alloys. Int. J. Impact Eng. 24, 747–758.

Wei, Z., Yu, J., Li, J., Hu, S., 2001. Influence of stress condition on adiabatic shear localization of tungsten heavy alloys. Int. J. Impact Eng. 26, 843–852.

Woodward, R.L., O'Donnell, R.G., 2000. Tensile rupture of tungsten alloys by the cascade of crack nucleation events. J. Mater. Sci. 35, 4067–4072.

Xu, X.-P., Needleman, A., 1994. Numerical simulations of fast crack growth in brittle solids. J. Mech. Phys. Solids 42, 1397–1434.

Yih, S.W.H., Wang, C.T., 1979. Tungsten: Sources, Metallurgy, Properties, and Applications. Plenum Press, New York.

Zamora, K.M.O., Sevillano, J.G., Pérez, M.F., 1992. Fracture toughness of W heavy metal alloys. Mater. Sci. Eng. A157, 151–160.

Zhou, F., Molinari, J.F., 2004. Dynamic crack propagation with cohesive elements: a methodology to address mesh dependency. Int. J. Numer. Methods Eng. 59, 1–24.

Zhou, M., 1993. Dynamic shear localization in a tungsten heavy alloy and ductile rupture in a spheroidized 1045 steel. Ph.D. Thesis, Division of Engineering, Brown University.

Zhou, M., 1998. The growth of shear bands in composite microstructures. Int. J. Plast. 14, 733–754.

Zhou, M., Clifton, R.J., 1997. Dynamic constitutive and failure behavior of a two-phase tungsten composite. J. Appl. Mech. 64, 487–494.

Zhou, M., Clifton, R.J., Needleman, A., 1994. Finite element simulations of shear localization in plate impact. J. Mech. Phys. Solids 42, 423–458.

Zikry, M.A., Kao, M., 1996. Inelastic microstructural failure mechanisms in crystalline materials with high angle grain boundaries. J. Mech. Phys. Solids 44, 1765–1798.